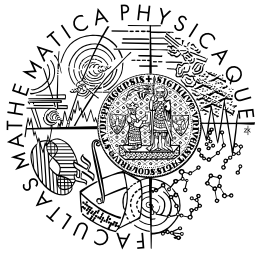

FACULTY
OF MATHEMATICS
AND PHYSICS
Charles University

MASTER THESIS

Tatiana Výbošťoková

Effects of solar activity in power-distribution grids

Astronomical Institute of Charles University

Supervisor of the master thesis:	doc. Mgr. Michal Švanda, Ph.D.
Study programme:	Physics
Study branch:	Astronomy and Astrophysics

Prague 2019

I declare that I carried out this master thesis independently, and only with the cited sources, literature and other professional sources.

I understand that my work relates to the rights and obligations under the Act No. 121/2000 Sb., the Copyright Act, as amended, in particular the fact that the Charles University has the right to conclude a license agreement on the use of this work as a school work pursuant to Section 60 subsection 1 of the Copyright Act.

In ..... date ..... signature of the author

First of all, I would like to thank my supervisor, doc. Michal Švanda for his overall help and willingness. In addition, I would like to thank all four distributors of the electric energy in the Czech Republic for the provided data and the Institute of Geophysics of the Czech Academy of Science for free availability of measurements from Budkov.

Title: Effects of solar activity in power-distribution grids

Author: Tatiana Výbošťoková

Institute: Astronomical Institute of Charles University

Supervisor: doc. Mgr. Michal Švanda, Ph.D., Astronomical Institute of Charles University

Abstract: Eruptive events on the Sun have an impact on immediate cosmic surroundings of the Earth. Through induction of electric current also affect Earth-bound structures such as the electric power distribution networks. Inspired by recent studies we investigate the correlation between the disturbances recorded by the Czech electric-power distributors with the geomagnetic activity represented by the K index.

We found that in the case of the datasets recording the disturbances on the power lines with the high and very high voltage levels and disturbances on electrical substations, there was a statistically significant increase of failure rates in the periods of maxima of geomagnetic activity compared to the adjacent minima of activity. There are hints that the disturbances are more pronounced shortly after the maxima than shortly before the maxima of activity.

Our results provide hints that the geomagnetically induced currents may affect the power-grid equipment even in the mid-latitude country in the middle of Europe. A follow-up study that includes the modelling of geomagnetically induced currents is needed to confirm our findings.

The second part of our research includes modelling of geoelectric field using one-minute geomagnetic measurements from Intermagnet database. We applied this model to the long-term measurements of the geomagnetic field during the period of increased solar activity (for example in days when aurora was observed) and considered possible destructive effects on the distribution network infrastructures. Using geoelectric field we computed currents that are induced in these infrastructures. Their values varied in order of tens of amperes. Thus we got a strong hint for effects of geomagnetic activity even in the mid-latitude country such as the Czech Republic.

Keywords: solar activity, geomagnetic activity, disturbances, Czech power grid, geoelectric field, geoelectric currents

Contents

Introduction

The spaceweather disturbances are mainly triggered by events associated with the solar activity. They may impact Earth's climate, man-made technological systems and disturb communication and GPS signals. Moreover, the electric currents induced in the modern technological systems generated by geomagnetic storms (known as geomagnetically induced currents or GICs) can disrupt or damage the transformers of the high voltage power grids, or alter the pipe-to-soil voltages in oil or gas pipelines.

Such harmful effects have been usually observed at high geomagnetic latitudes (Canada, Scandinavia) where the auroral electrojet flows in the ionosphere. This area is dominant by auroral ionospheric currents, where the ground magnetic field amplitudes change the most.

Even though significant GIC has been measured in mid-latitude area such as UK [Beamish et al., 2002], Spain [Torta et al., 2012], New Zealand [Marshall et al., 2012] and China [Zhang et al., 2015] and even in low latitude areas around the equator [Kappenman, 2003]. Transformer failures were reported even in South Africa [Gaunt and Coetzee, 2007]. These hints leading to a hypothesis that such effects are expected in the Czech Republic as well.

Despite the known effect of increased solar activity on space technology or the Earth itself, only a few researches related to this issue has been done so far. Most of the available work deals with the immediate effects registered on the infrastructure during or shortly after significant disturbances in solar activity. Most of them describe Hydro-Quebec blackout in 1898 caused by 13 and 14 March superstorm [Bolduc, 2002]. Recently, research has been focused on a long-term impact of fluctuating solar activity on the network infrastructures, even in cases of less important events than Quebec blackout [e.g Schrijver and Mitchell, 2013]. For example, there is study by Zois [2013] focused on the Greek electric grid and the disturbances on its key components.

One of the aims of this work is to make comparable analyzes for disturbances recorded in a Czech distribution network and determine the relationship between the failures of the grid components and increased geomagnetic activity in the Czech Republic. This relationship may tell us more about the statistical significance of the failure rates within geomagnetic active days. Anyhow, we still do not know much about the causality.

In this manner, we model the geoelectric field from which GIC can be computed. However, this includes more information about power transmission network than we are able to gain from distributors in the Czech Republic e.g., network admittance matrix, direction of the transmission lines. In such case, we were able to compute only currents which enter transmission infrastructure so we have a good estimate of GIC values flowing in the Czech power grid. This rough estimation is still a good indicator of the level of the increased solar activity effects in power-distribution grids.

The prediction of the occurrence of solar flares and CME is crucial as even small changes in solar activity can adversely affect the Earth 's conductive systems and telecommunications. Because of that, a probabilistic assessment of the likelihood of such events and their strengths is necessary. To be able to forecast

space weather we first need to understand physics behind it from coronal heating problem to interactions of the supersonic solar wind with Earth 's magnetosphere and following effects on near Earth-space environment.

In this study, we present the first detailed statistical analysis of the effects of solar activity in the Czech Republic.

1. Theory

1.1 The Sun

The Sun is the closest star to the Earth and with its parameters

- weight $M = (1.9891 \pm 0.0012) \times 10^{30}$ kg,
- radius $R = 695\,980$ km,
- luminosity $L = 3.86 \times 10^{26}$ W,

is the dominant body of the Solar system. However, its influence is not limited only to the gravity force that controls the movement of all bodies in the Solar system, we must also consider the influence of the solar plasma which fills an interplanetary space. The corona (the upper layer of the Sun's atmosphere) has a temperature up to 2 MK and constantly expands into the interplanetary space in the form of the solar wind. It consists of charged particles such as ions, protons and electrons which may hit the Earth.

It is the only star which can be observed in a great detail in relatively high spatial and temporal resolutions simultaneously 24 hours a day.

1.1.1 Structure of the Sun

The interior of the Sun can be separated into four regions by the different processes that occur there for example see Figure 1.1.

- **Core**, the innermost 25% of the Sun's radius, where temperature (15 MK) and pressure are sufficient for hydrogen nuclei to be fused into helium nuclei, providing the energy for the solar luminosity and for most of the activity in the outer layers. This energy ultimately leaves the surface as visible light. During the nuclear fusion, neutrinos are produced. They pass through the overlying layers of the Sun and can be detected here on the Earth and tell us more about the core.
- **Radiation zone**, from the edge of the core, the energy is transported outward by radiative diffusion. Photons propagate, are absorbed and remitted here [Brož and Šolc, 2013]. Although the photons travel at the speed of light, they bounce so many times through this dense material that a photon takes about a million years to finally reach the interface layer [Mitalas and Sills, 1992]. Radiation zone extends to 0.71 $R_\odot$, as was revealed from surface oscillations. The temperature decreases from 7 MK to 2 MK.
- **Tachocline** is the thin layer where probably magnetic field is generated by a magnetic dynamo. The changes in fluid flow velocities across the layer can stretch magnetic field lines of force and make them stronger [Spiegel and Zahn, 1992].
- **Convective zone** is the outermost layer of the solar interior that extends to the visible surface. The surface temperature reaches 6000 K which enables

heavier ions to recombine with electrons, material becomes more opaque and energy is transported through convection. The convection sets in when the temperature gradient is larger than the adiabatic gradient, material that move upward will be warmer than its surroundings and will continue to rise further. The fluid expands and cools as it rises [Karlický, 2014].

Solar atmosphere consist of four layers:

- **Photosphere** is the lowest atmospheric layer and emits most of the energy released in the core. Solar plasma becomes transparent to optical light here. The thickness of the photosphere is about 300 km. Convective motions are observed in the photosphere as a granulation, a cell structure with a mean size of few thousand kilometers. Ion of hydrogen H^- plays an important role here since its ionization energy is quite low and it can be ionized by optical or IR photons. H is the main source of the opacity. On the other hand, its recombination produces most of the photons which escape from the Sun [Brož and Šolc, 2013]. The temperature reaches its minimum at 4300 K and surprisingly rises further from the solar surface.

- **Chromosphere** is an optically thin layer, 2000 km thick [Brož and Šolc, 2013]. The temperature rises to 20 000 °C which is a good condition for the formation of the Balmer H lines (Hα line) or lines of ionized calcium Ca II (H and K line). The chromospheric plasma can penetrate into the upper atmosphere as prominence (closed plasma cloud) [Karlický, 2014].

- **Transition region** is only a few hundred kilometers thick layer where temperature rises from 20 000 °C to a few million degrees on the border with the corona. Emission lines are in the extreme ultraviolet part of spectra. Most important are the Lyman α line of hydrogen and the lines of partially ionized heavier elements such as O IV, C III and Si IV [Mariska, 1992].

- **Corona** is the outermost layer of the solar atmosphere visible during the solar eclipse. The temperature reaches more than 1 MK here so most of the thermal energy radiated by coronal plasma is in the form of soft X-rays and EUV line emission mainly created by strongly ionized heavier elements e.g., carbon or iron. The corona extends millions of kilometers into outer space. Beyond 1.5 $R_\odot$ the magnetic field lines do not return within the heliosphere and plasma is not bound anymore thus flow outwards and forming the solar wind. During the minimum of the 11-year magnetic cycle, the corona extends outward from the low latitude regions near the Sun's equator. During the solar maximum dense regions called streamers are more regularly distributed around all latitudes on the Sun [Koskinen and Vainio, 2009].

1.2 Solar activity

The Sun consists of hot plasma interwoven with magnetic fields. These fields are created and amplified in the outer envelope of the solar body, rise and blend through the solar atmosphere. Because the outer envelope of the Sun is very

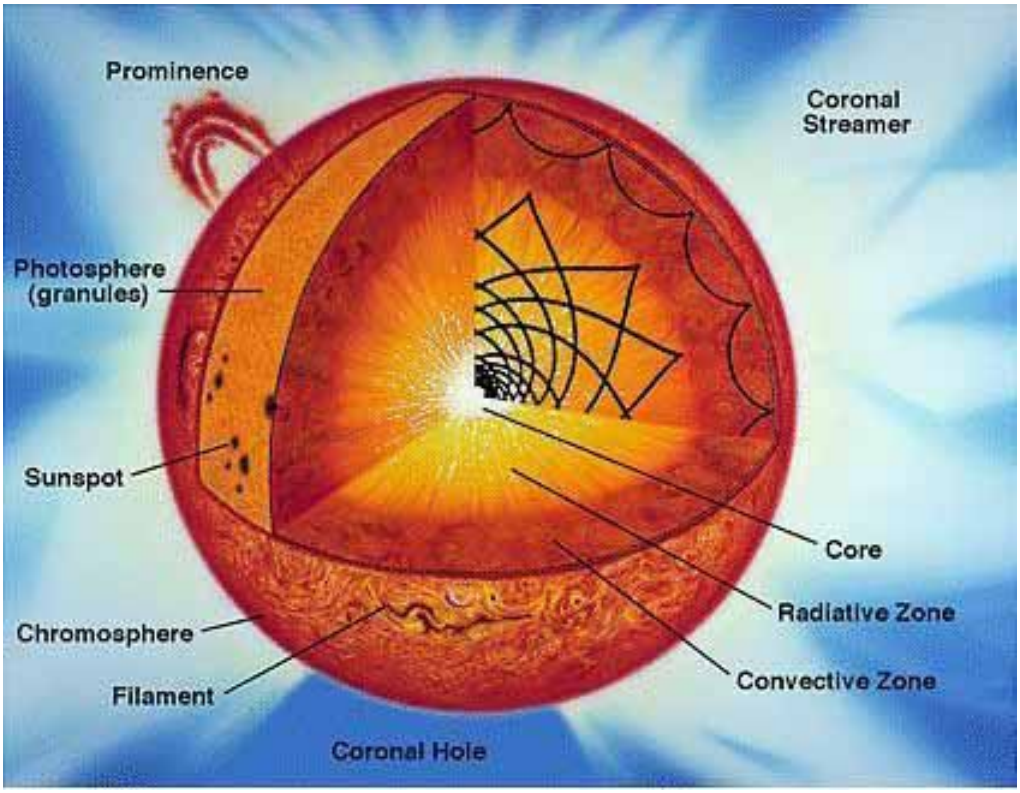

Figure 1.1: Structure of the Sun. (NASA, https://www.nasa.gov)

dynamic (mainly due to convection), the magnetic fields change with time as well. The phenomena associated with the existence and variability of the localized magnetic field are called *solar activity*. Solar activity includes phenomena such as sunspots, prominences, solar flares or CMEs. Prominences and coronal disturbances are often associated with sunspots, but there are also solar activity phenomena which do not involve sunspots directly, such as the appearance of magnetic flux tubes and variations in the global solar magnetic field. Violent phenomena such as solar flares and coronal mass ejections may potentially have a dramatic impact on the Earth's environment.

Besides the effects of solar flares and CME that are relevant for space weather magnetic variability of the Sun causes flux variation in UV an X-ray as well as in total irradiance and the flux of cosmic rays hitting the Earth's atmosphere, all of which may affect the terrestrial climate [Friis-Christensen, 2000].

The solar magnetic field is variable on all temporal and spatial scales on which it has been observed so far. The timescales range from minutes to centuries with different physical processes driving these variations. Magneto-convection (the interaction of magnetic field and convective motions) causes a variability on timescales between minutes and days. Variations of active regions and global flux transport over the solar surface changes from days to several days, whereas dynamo process and its long-term modulations cover the timescales of decades and centuries.

The most important timescale of solar magnetic activity is the 11-year activity cycle (or 22-year magnetic cycle) of active regions and sunspots. Most recently it has been acknowledged that the solar cycle length varies between 9 to 12 years

[Benestad, 2006]. Period of the greatest solar activity during the 11-year solar cycle of the Sun is called the solar maximum which includes, for example, large numbers of sunspots, solar flares, and growth in the solar irradiance. On the other hand, solar minimum is the period of the least solar activity. During the solar minimum solar flares activity and sunspots are less often and sometimes does not occur for days. As it was shown by Richardson et al. [2001] even during solar minima there are CMEs strong enough to have a certain impact on the Earth and its surroundings.

1.2.1 Solar flares

A solar flare is an explosive phenomenon observed in the solar atmosphere. Flares occur in regions where there is a rapid change in the direction of the local magnetic field. The favored mechanism to explain it is the magnetic reconnection. It is the most efficient mechanism of releasing magnetic energy of 10^{22} to 10^{25} J in the form of the radiation, kinetic, thermal and non-thermal energy [Shibata and Magara, 2011].

The first flare was observed in white light by Carrington in 1859 but only large flares can be observed in the visible continuum. More characteristic for the flares, especially chromospheric flares, is a H_α line emission [Benz, 2017].

During flare event electrons are accelerated typically to energies of 10 to 100 keV, sometimes up to 10 MeV, and the highest energy of which nuclei can reach is in order of MeV or even GeV [Malandraki and Crosby, 2018]. Emission of the solar flares range from radio waves to γ-rays.

The appearance of flares tends to follow a general rule:

1. a rapid increase in the intensity,
2. followed by a brief period (often less than a one minute) of maximum activity,
3. a slow decay.

In the preflare phase the coronal plasma in the flare heats up and is visible in soft X-ray and extreme UV. Most of the particles are accelerated during the impulsive phase (a maximum activity phase) when also most of the energy is released. Some particles are trapped and produce radio emission, some bombard denser layers of the solar atmosphere below the flare and some of them are directed into the interplanetary space. In the decay phase in the high corona, plasma ejections or shock waves continue to accelerate particles. The flux of high-energy particles and cosmic rays are increased near the surface of the Earth as a consequence of the solar flare [Shibata and Magara, 2011].

1.2.2 Coronal mass ejections

Coronal mass ejections (CMEs) are large plasma magnetic clouds, torn off from the Sun, observed in the solar corona. Example of such eruptive event can be seen in Figure 1.2. They originate from the closed field line regions, which opened locally during the process of their formation. A typical CME carries off about

$10^{12} - 10^{13}$ kilograms of solar mass and its angular size is about $40 - 50°$ [Antia et al., 2003].

The speeds of CMEs fall in a broad range from about 20 km/s to more than 2000 km/s [St Cyr et al., 1999]. Around 1 AU the speed drops below 750 km/s and it is never smaller than a minimum solar wind speed (350 km/s) which means that the faster CMEs are decelerated and slower ones are accelerated toward the solar wind speed Schrijver and Zwaan [2008].

The CME does not radiate, the faint light observed by coronographs coming from the Thompson scattering of solar photons on electrons in the cloud. The white light brightness varies with electron density but not with temperature, thus of what density can be determined.

The occurrence rate of CMEs is connected with the solar cycle. During the solar maximum, there are $\sim 4 - 5$ events per day and only about one ejections every fifth day appears during a minimum of a solar cycle. During the minimum CMEs usually appear around the equatorial region of the Sun. Their structure becomes more complicated when the Sun is active.

Both ends of the magnetic field line of CME can be still tied to the Sun even at a distance of 1 AU. We can also see completely detached CMEs but most usual are structures with only one end tied to the Sun [Malandraki et al., 2003]. This contributes to the necessity of a better understanding of the relationship between reconnection and cutting field lines.

The effect of the CME hitting the Earth's magnetopause depends on whether the magnetic field in front of it points toward the north or south. The strongest effect happens when the field points toward the south, the day-side reconnection opens the magnetopause and the excessive energy and plasma penetrate into the magnetosphere [Case et al., 2017].

Unfortunately, we do not know much about the origin of CME. There are models supporting connection with the solar flare. However, only about 40% of CMEs have been associated with flare close to the site of the ejection. Although these flares may take place before, simultaneously or after the rise of the CME. Another explanation may be associated with eruptive prominences. In this case, there is a problem with observing prominence (using coronograph, very rarely with situ spacecraft in the solar wind close to the Earth) and CME at the same time.

1.2.3 Solar energetic particles

Both flares and CMEs accelerate charged particles to higher energies. Electrons accelerated by solar flares can occasionally reach energies of 100 MeV. However, their typical energy is in order of 100 keV. On the other hand, protons may have energies up to 1 MeV. They are distributed in all directions and are sources of X-rays, γ rays as they collide with other solar particles, some produce radiowaves through radio emission processes and some of them can escape from the Sun and thus reach the Earth.

Fluxes of charged particles are much less ($\sim 10^{-5}$) than the flux of the solar wind. They are trapped into the magnetic field lines forced to follow magnetic field lines. This is how the solar energetic particles (SEPs) reach the Earth.

There are two types of SEPs, gradual and impulsive, both of them accelerated

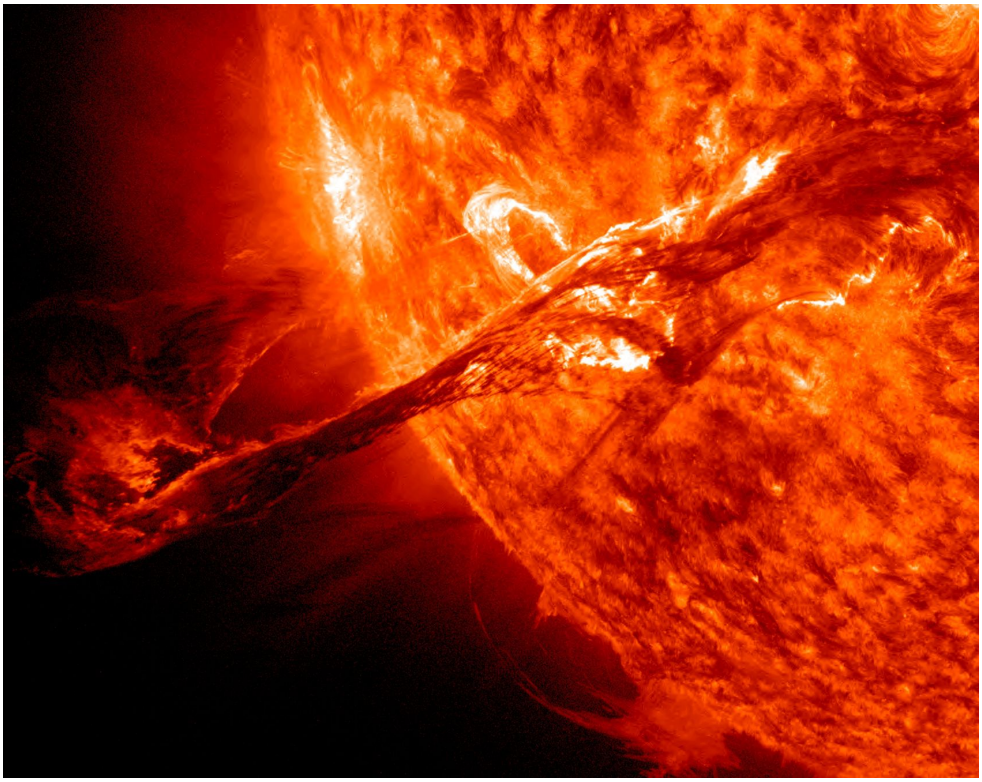

Figure 1.2: Coronal mass ejection. (NASA, https://www.nasa.gov)

through different processes.

Impulsive SEPs are accelerated during the impulsive phase of a solar flare. They reach energies of GeV, last a few hours and are best observed when the observer is magnetically connected to the flare site. Enhancement in ^{3}He/^{4}He ratio of by factor $10^3 - 10^4$ means that acceleration mechanisms have to be very efficient in the acceleration of these particular elements.

On the other hand, gradual SEPs are connected with CME 's shock waves thus having a longer duration (several days) and are proton-rich. They have to be accelerated in the solar corona because of its high energy that reaches hundreds of MeV [Malandraki and Crosby, 2018].

1.2.4 Solar wind

The space between the Sun and its planets is filled by a tenuous magnetized plasma, which is a mixture of ions, protons, electrons and α particles flowing away from the Sun called the solar wind [Bame et al., 1977]. Most of the solar wind originates from coronal holes, regions of low density, nearly vertical magnetic fields and darkness in soft X-ray pictures. This outermost layer extends far beyond the Earth 's orbit and gradually changes into the interplanetary medium, until it meets the interstellar medium at the heliopause located from 100 to 200 AU.

There are two types of the solar wind, one called fast solar wind, more tenuous and flowing with speed about 750 km/s and a denser and slower one with speed about 350 km/s. We still do not know the physics behind it as well as details of their source regions. However, it is believed that the fast solar wind originates from coronal holes at high solar latitudes whereas the slow wind emerges wherever

the field lines are largely closed low in the corona [Schrijver and Zwaan, 2008]. CME can be considered as a third independent solar wind type.

As the solar wind expands, its density decreases with distance from the Sun. At some point the distance is so large that the solar wind can no longer push back the fields and particles of the local interstellar medium and the solar wind slows down from its average speed of 400 km/s to 20 km/s. This transition region is called the termination shock. Its position is still unknown but must be more than 50 AU as was shown by direct measurements [Hanslmeier, 2010]. This is the challenge for modelers since it does not correspond to an equilibrium configuration along magnetic field lines but instead originates from coronal domains where the connectivity appears to evolve on a time scale of only a few hours.

To be able to make a proper model of space weather, we first need to have a proper model of the solar wind. Chemical composition of the solar wind can tell us more about its origin, i.e. the source. Composition of solar wind is different from the composition of the solar surface and shows variations that are associated with solar activity and solar features as was showed in Wimmer-Schweingruber et al. [2001].

Around solar maximum, the structure of the solar magnetic field is much more complicated and reduction of the polar coronal holes are observed. On the other hand, there are more smaller-scale opening and closing structures at lower latitudes. This makes also the solar wind structure more variable, which in turn drives magnetic activity in the terrestrial environment. Indeed the solar wind is neither steady, isothermal, nor radially expanding. The magnetic field affects its structure dramatically.

1.2.5 Corotating interaction regions

When a fast solar wind stream, originating in a coronal hole, interacts with the ambient slower solar wind due to the rotation of the Sun, a long lasting and large scale region in the heliosphere is formed. This region of the compressed plasma, increased density and magnetic field is called the corotating interaction region (CIR). They can last for several solar rotations. This interaction usually takes place in the inner heliosphere hence CIR is usually formed around 1 AU from the Sun. Both ends of CIR expand into the interplanetary solar wind at the sound speed as a result of increased pressure. The front edge of the CIR is called a forward wave and the trailing edge is called a reverse wave. There is a pressure gradient due to these weaves that force the slow solar wind to accelerate ahead of the stream and decelerate fast solar wind within the stream in order to transfer the energy and momentum from the fast solar wind to the slower one and make the discontinuity smaller.

When the difference in speed between the fast and slow solar wind is twice the sound speed the interaction region steepens slower than the stream. This leads to the compression of the interaction region with distance from the Sun and non linear rise of pressure occurs. Shock wave is created from the forward and reverse wave which bounds the interaction region. The shock wave propagates faster than the sound speed so CIR can expand. CIRs are usually bounded by the shock wave around 3 AU, although, some of them can be bounded even at 1 AU. At greater distances larger fraction of the magnetic field and mass are founded

in the interaction regions Gosling and Pizzo [1999].

When the instability occurs the triggered shock wave causes disruption of the Earth's magnetosphere [Heber et al., 1999] which usually happens beyond 1 AU. However there are cases when geomagnetic storms were caused by CIR [Richardson et al., 2006] meaning this had to happen before 1 AU.

Since z component of the interplanetary magnetic field fluctuates within the CIR, we can observe the irregular profile of the main phase of geomagnetic storms. Similar to the decay phase which has an unusual longer duration in the range from days to weeks [Tsurutani and Gonzalez, 1997].

1.3 The interplanetary magnetic field

When the magnetic Reynolds number is much larger than a unity $R_m \gg 1$ which means fluid (plasma in our case) with very small resistivity, we have a situation of magnetic field frozen into this fluid. Under such conditions, that hold in the solar corona and further (collisionless plasma), plasma cannot change from one field line to another if it is perpendicular to magnetic field lines but can move freely along them. Either the field lines have to follow the motion of plasma (weak field, no significant Lorentz force) or the magnetic field suppresses the motion perpendicular to the field lines (strong field, dominating Lorentz force).

The solar wind carries the magnetic field from the Sun to the interplanetary space until it reaches the heliopause. This interplanetary magnetic field (IMF) is governed by electric currents in the solar wind.

The IMF originates in regions of open magnetic field on the Sun. The direction of the field is opposite in the Sun's northern and southern hemisphere. Along the plane of the Sun's magnetic equator, the oppositely directed open field lines run parallel to each other and are separated by the interplanetary current sheet.

As a consequence of the Sun's rotation, the IMF has a spiral shape which is called the Parker spiral. Structure of the IMF varies significantly from the ecliptic to the poles. Close to the Sun, the plasma rotates with the Sun but in the radial expansion, the field is wound to a spiral. Between the equatorial plane and the polar direction, the field gets a helical structure. At 1 AU the equatorial spiral angle is about 45° [Parker, 1958].

Since interplanetary magnetic field is a vector it has three components B_x, B_y, B_z. B_x and B_y are oriented parallel to the ecliptic. The third component B_z (north-south component) is perpendicular to the ecliptic.

1.4 Space weather

The activity on the Sun's surfaces such as flares, CME or solar energetic particles creates the space weather. This term refers to conditions on the Sun, in the interplanetary plasma and in the interplanetary magnetic field that has potential riskri to influence the performance and reliability of both space-borne and ground-based technological systems and even endanger human life or health through radiation exposure.

Through interaction of SEPs with the Earth's magnetic field plasma particles are accelerated to regions of the magnetic south and north poles. They collide

with atoms and molecules in the high-altitude atmosphere which results in light emission called polar light or aurora.

The escaping plasma from the solar corona carries solar magnetic field along, out to the border of the heliosphere where its dominance finally ends. The heliosphere is a vast region of space surrounding the Sun and the solar system that is filled with the magnetic field and charged particles. Coronal holes are sources of long-lived solar wind high-speed streams Krieger et al. [1973]. They are usually located above inactive parts of the Sun where open magnetic field lines prevail.

The solar wind and IMF carried with it connect the solar atmosphere with the Earth. The Earth itself is not affected by solar wind directly since its impact is largely shielded by the Earth's magnetosphere. Particles of the solar wind cannot penetrate unless magnetic reconnection of interplanetary (IP) and planetary magnetic field lines occurs see Figure 1.3. This happens when IMF and geomagnetic field lines are oriented antiparallelly (the direction of B_z turns southward), resulting in a transfer of energy, mass, and momentum from the solar wind to magnetosphere.

The reconnection of IP and geomagnetic field lines usually takes place on the day-side of the Earth transforming the closed magnetic structure to an open field with one end connected to the Earth and the other attached to the solar wind. These reconnected open field lines move towards Earth's night-side where they stretch, due to solar wind drag. Another reconnection takes place on the night-side, where magnetic lines anchored in the Earth join up forming a new closed-loop structure. The closed magnetic field must return to the day-side where new reconnection begins. This convective process extracts kinetic energy from the solar wind and let plasma to enter, so geomagnetic storms may occur [Cowley, 1973].

Furthermore, there are shock waves produced by propagating CMEs which may disturb the Earth's magnetosphere. Since the speed of CMEs is greater than the normal speed of the solar wind, which through CME propagate, large shock waves are produced. Disturbances in the solar wind caused by these shock waves arrive to the Earth a few days after leaving the Sun and cause disturbances in the geomagnetic field. Disturbances in the solar wind can be caused by solar wind stream interaction regions (SIR) as well. However, the effects associated with disturbances driven by the CME and by solar wind SIR are different near the Earth.

As it was mentioned when interplanetary CME moves supersonically with respect to the ambient solar wind, an interplanetary shock is created. This lead to an enhance of the density, magnetic field induction and velocity and sheat region is created (accumulated solar wind in front of the CME). B_z of the IMF is enhanced due to deflection of the magnetic field from the ecliptic. Propagation of the shear region evolves into coronal ejecta which increases both speed of the plasma and southward component of IMF and so has a greater effect in terms of geomagnetic storms.

In contrast, it is not usual that the SIR is accompanied by shocks at 1 AU. They have a smaller and fluctuating B_z component reappearing with 27 day rotation period of the Sun. In general, they have a smaller effect on the Earth than the disturbances triggered by fast CME [Luhman, 1997].

Shock waves which propagate away from the Sun caused by these disturbances

in the solar wind can penetrate through interplanetary space and thus reach the Earth. They compress the magnetic field on the day-side of the Earth whereas the field on the night-side is stretched out. The Earth 's geomagnetic field usually has a dipole structure, which means that the field lines emerge from the magnetic south pole and meet at the magnetic north pole where they penetrate the Earth's surface

Another cause of space weather are gradual SEP events which radially expand outward from the Sun and may be directed to the Earth. Impulsive SEPs propagate along open magnetic field lines and escape into the IP medium. These impulsive SEP events are more frequent but not as important as gradual SEP events in terms of space weather [Malandraki and Crosby, 2018]. They present a constant danger for astronauts and satellites outside the magnetosphere in terms of increased radiation.

Several factors connected to CIR can cause disturbances in geomagnetic activity [Belcher and Davis Jr, 1971]:

1. **Compression of the geomagnetic field**. The stronger the magnetic field, the larger B_z component is. In the case of negative z-component, there is a reconnection of IMF with magnetic field lines of the Earth .

2. **Increased fluctuations of IMF**, caused by shear in the velocity. Larger fluctuations cause stronger disturbance in geomagnetic activity.

3. **Alfven waves in fast streams**. Again, the negative B_z component of IMF associated with portions of the waves are important for geomagnetic activity.

4. **High solar wind velocity**, together with strong southward B_z oriented increase geomagnetic activity.

1.5 Geomagnetic activity

About 100 km above the Earth's surface, the amount of ionized gas becomes appreciable. Since ionized gas is made of electrically charged particles, it feels the Earth's magnetic field, which guides the motion of charged particles in near-Earth space. Through their interaction with the magnetized solar wind, the solar-activity disturbances induce disturbances in the magnetosphere, called the *geomagnetic activity*. Significant fluctuations of the geomagnetic activity are called *geomagnetic storms*.

1.5.1 Geomagnetic storms

Geomagnetic storm (GS) has three phases:

1. **initial phase**, also referred to as storm sudden commencement, starts with a sudden increase in the horizontal component of the geomagnetic field in tens of minutes. However not every geomagnetic storm has the initial phase.

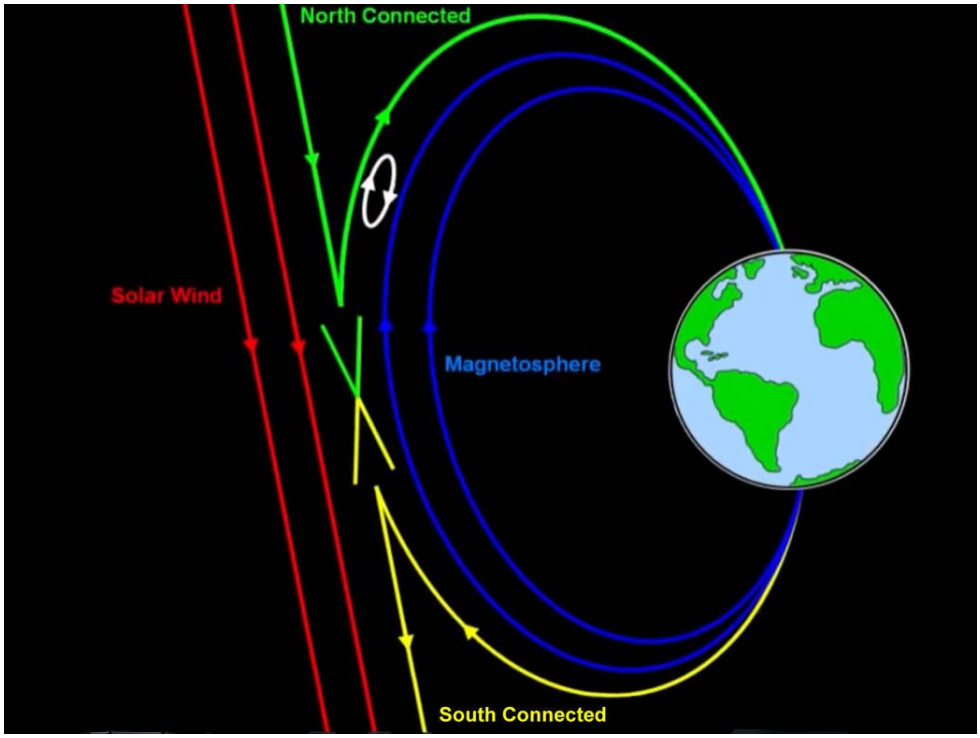

Figure 1.3: Magnetic reconnection in the Earth 's magnetosphere. (NASA, https://www.nasa.gov)

2. **main phase** has a longer duration varying from hours to days. Charged particles penetrate deeper into the magnetosphere and perturb there the ring current which is an electric current carried by charged particles trapped in magnetosphere.

3. **recovery phase** occurs when the IMF turn northward again. The rate of charged particles deep in the inner magnetosphere decreases and DST (see section 1.5.2) index reaches its minimum.

Two types of GS exist:

1. **recurrent geomagnetic storm** can be observed every 27 days which is a duration of the mean solar rotational period. It is caused by the interaction of CIR with the Earth and is more usual during solar minimum.

2. **non-recurrent geomagnetic storm**, on the other hand, sets in near increasing phase of the solar cycle. Interplanetary disturbances caused by CMEs (both interplanetary shock wave and ejection) are their main source.

1.5.2 Indices of geomagnetic activity

The level of geomagnetic activity can be most easily expressed by measuring the Earth's magnetic field strength. From the measured geomagnetic field and its evolution in time a variety of indices of geomagnetic activity may be constructed. The information about the current state is given by DST index (Disturbance Storm Time index) characterizes the mean value of disturbance averaged over

ΔB [nT]	0	5	10	20	40	70	120	200	330	500
K	0	1	2	3	4	5	6	7	8	9

Table 1.1: Conversion of maximum fluctuation ΔB to K index for NGK observatory (Germany). Similar table was used to compute the K index for Budkov Observatory.

one hour. DST measures strength of the ring current around the Earth. Negative DST values indicate attenuation of Earth's magnetic field and it is usually used to classify an ongoing geomagnetic storm. If the DST amplitude is within 50 nT the storm is weak, in a range from 50 to 100 nT medium storm occur, a strong storm has DST index from 100 to 250 nT and finally 250 nT and more is classified as a superstorm.

K index is a semi-logarithmic quantity describing changes in the amplitude of the horizontal component of Earth's magnetic field over a three-hour interval. K index method defines irregular variations as the range (difference) between the upper and lower fitting quiet daily curves during each three-hour interval. When $K = 0$, then the geomagnetic field is in a quiescent state, $K > 5$ indicates the geomagnetic storm and $K = 9$ indicates the superstorm. Derivation of K index depends on the geographic location of the observatory. In practice, observatories at higher geomagnetic latitude require higher levels of fluctuation for a given K index. Table 1.1 represents the conversion between maximum fluctuations of the magnetic field $\Delta\ B$ in units of nanotesla and K index.

There is also a K_p index obtained from averaging K indices from several different observatories and ranges from 0 to 9 where a value of 0 means that there is very little geomagnetic activity and a value of 9 means extreme geomagnetic storming [Perrone and De Franceschi, 1998]. To calculate K_p the daily quite solar variation is removed from the measurements of magnetic field strength. Then the difference between the largest and smallest values is computed. The K_p index describing the global level of all irregular disturbances of the geomagnetic field caused by solar particle radiation within the 3-hour interval concerned. It is important to understand that this K_p index is not a forecast or an indicator of the current conditions, it shows the K_p value that was observed during a certain period.

Depression in galactic cosmic ray (GCR) intensity caused by the magnetic field of plasma in interplanetary space which sweeps out the galactic cosmic rays away from the Earth is called Forbush decrease (FD) [Forbush, 1937]. It starts with a sudden decrease in GCR intensity within about a day and a gradual recovery phase lasting several days. Typical sources of FD are transient interplanetary events such as CMEs or CIRs. Disturbances in solar wind parameters e.g., proton speed, density, and temperature together with fluctuation of IMF trigger a decrease in galactic cosmic ray flux. FD can be observed using particle detectors and used as a good indicator of geomagnetic activity caused by solar activity events.

1.5.3 Effects of geomagnetic activity

Solar flares release flashes of radiation covering wavelengths from radio to gamma rays that can e.g., heat up the Earth 's atmosphere within minutes such that satellites drop into lower orbits.

Solar energetic particles accelerated to near relativistic energies during major solar storms arrive at the Earth 's orbit and may among other endanger astronauts outside the Earth 's protective magnetosphere. Besides the heavy protons from galactic cosmic rays, protons from SEPs ionize the Earth's atmosphere too which can last from hours to days and are the main source of ionization in the mid and low atmosphere. There is some hint of its impact on the aerosol structure in the atmosphere or clouds formation and its further affection of the climate [Usoskin et al., 2009]. However, its effects on the climate are still not clear.

CME ejected into interplanetary space hit the Earth within a few hours or days and may cause geomagnetic storms. Geomagnetic storms affect human infrastructure. The affection of the ion formation and recombination in the ionosphere disturbs the propagation of radio waves transmitted through the ionosphere [e.g. Tsurutani et al., 2009].

The interplanetary CME creates a shock wave that compresses Earth's magnetosphere. Together with the solar energetic particles, the CME shock wave causes changes in the system of currents of the magnetosphere and ionosphere that generates a time-varying electric field see [Koskinen et al., 2001]. This geoelectric field, in turn, gives rise to geomagnetically induced currents in the conductive structures on the Earth's surface.

The GICs arise due to voltage differences between the endings of grounded conductor and can produce damage in the system attached to the conductor such as railways [Eroshenko et al., 2010], pipelines [Pulkkinen et al., 2001] and particularly in power networks [Pirjola, 2000].

1.5.4 Effects of geomagnetically induced currents

The presence of GICs in the power grid may interfere with their normal operation and cause damage resulting in the failure or service disruption. GIC in power networks caused three main effects:

1. GIC may be treated like overvoltage that cause disconnection of the affected part of the distribution network. This, in practice, means that the total power transmitted by the network is now directed to fewer branches. This may affect the safety feature on another branch and so on until there is not enough wiring/electric lines connected to the network function. Cascading power grid failure is triggered.

2. Since GICs are time varying currents, their characteristic variability period is a few minutes, so they vary with frequencies by order of mHz. Since the transformer operating frequency is 50 Hz, GICs are essentially DC currents. This implies that if the GIC occurs in a transformer, it moves the hysteresis curve and saturates the core with one polarity. The transformer heats up, intermediate insulation is damaged, the field irradiates outside the core. Oil in the cooling bath degrades, gassing appears. In the extreme event, the transformer core may start melting.

3. The presence of GIC impacts the stability of the system frequency. Random fluctuations represent the load for generator turbines and lead to the formation of an unbalanced phase array due to the presence of reverse currents.

1.6 Historical records of geomagnetic storms

All of the effects of increased geomagnetic activity mentioned in previous chapters play a significant role in determining the conditions on the Earth and its surrounding. Some of them can have an adverse effect on the infrastructure and technology. There are evidences from the past that can prove it.

Server www.solarstorms.org aggregates archives newspaper articles dealing with increased geomagnetic activity. Obviously, it must have been a truly significant activity when it was also reported in mainstream daily newspapers. The archive contains 306 articles about 105 events since 1859, with 60 of these events recording effects on Earth technologies.

September 1, 1859, an events nicknamed "The Superstorm" was observed worldwide and it is one of the greatest events recorded in the last 150 years. Richard Carrington [Carrington, 1859] and Richard Hodgson [Hodgson, 1859] observed a white flare for the first time in history. The Earth was hit with a strong geomagnetic storm in the next two days [Cliver and Dietrich, 2013]. CME surpassed the Sun-Earth distance in 17.6 hours. This high speed occured probably only due to a series of previous CMEs that cleared the interplanetary space (as evidence Aurora was observed on 29 August). In Europe and in the United States, the telegraph network completely failed. Strong geomagnetic storms caused an aurora visible in sub-Saharan Africa, Mexico, or Indian city of Mumbai.

On May 15, 1921, the signalling and control system failed in the whole New York, soon it was following by a fire in the control tower on 57th Street and Park Avenue [Silverman and Cliver, 2001]. The system collapsed due to the presence of strong GICs. Cable communication was disturbed in most of Europe, a fire in the telephone centre was reported in Sweden.

Massive geomagnetic storm on 22 January 1938 caused problems on the railway corridor between Manchester and Sheffield. GICs penetrated into the signalling device and disable its functionality.

Astronomers tracking the active region 5 395 on the Sun spotted a massive cloud of super-heated gas on March 10, 1989. Three days later people around the world saw a Northern Lights. The solar flare that accompanied the outburst immediately caused short-wave radio interference. The magnetic disturbance created electrical currents in the ground beneath much of North America. On March 13, the currents entered the electrical power grid of Quebec. In less than 2 minutes, the entire Quebec power grid lost power for 12 hours. Two Salem power stations (New Jersey, USA) and one block of Hope Creek power plant were also affected. By passing the GIC with an estimated peak amplitude of 224 A, the cores of the enhancement transformers at Salem I and II blocks were severely damaged. It is worth mentioning that in the 25 months from the March 1989 storm, 12 transformers failed with different time delays in the United States. Adverse effects were observed in Europe as well.

On October 30, 2003, the GIC triggered an hour-long blackout in Malmö,

Sweden. The recorded GIC amplitudes were up to 300 A. Ten outages of various network devices were recorded in this area from 29 to 30 October (disconnection of transmission lines, disconnection of transformers) [Lundstedt, 2006].

It is clear that massive geomagnetic storms have an immediate impact on the stability and functionality of grids and installed facilities. The question of whether weaker geomagnetic storms could be spotted/monitored has been only answered recently. Works [Schrijver and Mitchell, 2013] and Schrijver et al. [2014] deal with statistics of disturbances in the North American grid as well as statistics of insurance claims related to grid operation. Both work independently concluded that 4% of all failures in the US network can be statistically associated with solar activity.

2. Data

Although disturbances in power grids associated with strong solar activity events are known in Europe, no one has done a long-term statistical study for European countries. There may be several reasons: for example, to carry out a large-scale study for a territory comparable to the United States is extremely difficult. Each European state has its own operator, which deals with disturbances according to its own internal regulations. To combine different datasets may thus be extremely difficult. We found that even for one country, the Czech Republic, the combination of various datasets from a group of power-network operators into one dataset is virtually impossible.

2.1 The Power Grid in the Czech Republic

The Czech Republic lies in the central Europe and is extended in the east–west direction (about 500 km length) compared to the "width" in the south–north direction (about 280 km). In terms of the electric power grid, the spine of the power network is operated by the national operator ČEPS, a.s., which maintains the very-high-voltage 400 kV, 220 kV and selected 110 kV transmission networks. It connects the Czech Republic with sixteen other members of the European Network of Transmission System Operators for Electricity (ENTSO-E). ČEPS also maintains the key transformers and electrical substations in the transmission network see Figure 2.1.

The area of the state is then split into three regions, where the electricity distribution is under the responsibility of the distribution operators. The southern part is maintained by E.ON Distribuce, a.s., the northern part by ČEZ Distribuce, a.s., and the capital city of Prague is maintained by PRE Distribuce, a.s. All three distributors maintain not only very-high-voltage (110 kV) and high-voltage (22 kV) power lines, but also connect the consumers via the low-voltage (400 V) distribution network.

2.2 Failure Logs

After years of delicate negotiations, we managed to obtain the maintenance logs from all the operators mentioned in the previous section. We obtained essentially the lists of disturbances recorded in the maintenance logs by the company technicians with their dates and many more details, which included also the probable cause of the failure. The lists contained not only the events of the equipment failure (e.g. defects), but also the events on the power lines, such as the repeated unplanned switching, power cuts, or service anomalies. By mutual non-disclosure agreement with the data providers, the datasets were anonymised and must be presented as such.

We first went through an extensive manual check of the obtained logs, when we excluded the events, for which the cause was unrelated to geomagnetic activity. That is we excluded the defects that occurred prior to putting the equipment into operation (i.e. manufacturing defects) or failures caused by other, space-weather

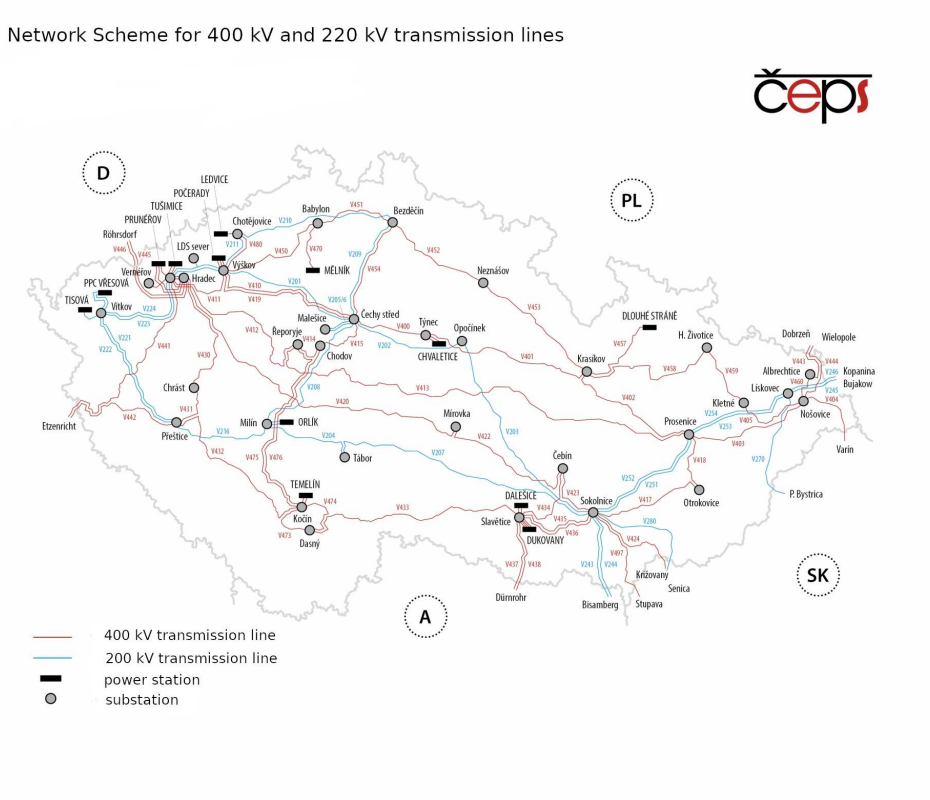

Figure 2.1: 400 and 220 kV power transmission system in the Czech Republic. (ČEPS, a.s.)

unrelated effects (traffic accidents, floods, etc.).

The inhomogeneous datasets were split into twelve subsets D1–D12, which were investigated separately. Each sub-dataset was selected so that it contained only events occurring on devices of a similar type and/or with the same voltage level and were recorded by the same operating company. The dataset descriptions are summarised in Table 2.1 and visualised in Figure 2.2. We aim to study only the failure rates so that from the logs we kept only the date on which the event occurred and did not consider any other detail. This reduction was done for two reasons. First, the number of events was quite low in most cases (a few hundred per year usually) and further splitting would lower a statistical significance. Second, the records in the log were quite inhomogeneous even within the same log, because the forms entering the database were filled by different persons. The final clean datasets are one-by-one compared with the level of geomagnetic activity using statistical methods.

2.3 Geomagnetic Activity

The selection of a proper index to assess the effects of solar/geomagnetic activity to power grids is a delicate issue [see the discussion e.g. in Schrijver and Mitchell, 2013]. We realised that none of the solar indices is suitable because events on the Sun (flares, CMEs) may have a different geoeffectivity. Still, the sunspots number or occurrence of X-class flares may serve as a secondary index to discuss various effects in the Sun-Earth connections.

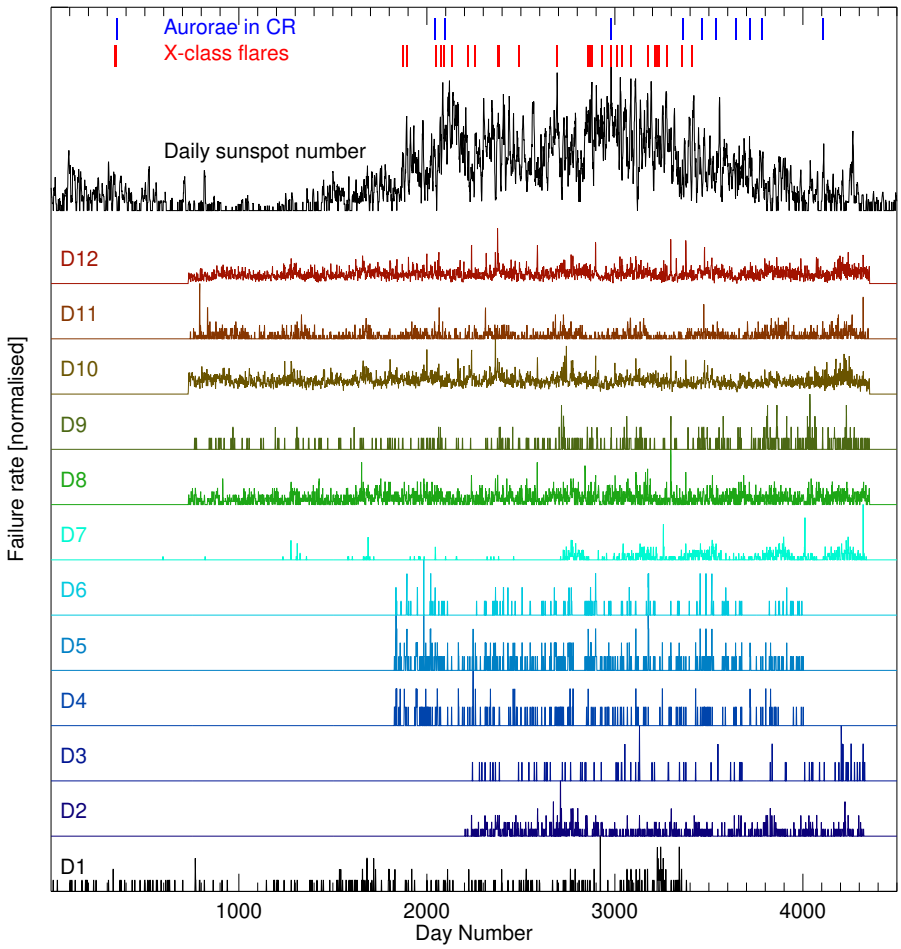

Figure 2.2: Failure rates as registered in the various datasets in time. The individual datasets were normalised to their maximum value. At the top of the figure we also plot the relative sunspot number for reference and indicate the dates, when X-class flares ignited and when aurorae were seen in the Czech Republic.

Dataset ID	Voltage level	Type
D1	very high voltage	equipment: transformers, electrical substations
D2	high voltage	equipment
D3	very high voltage	equipment
D4	high and low voltage	power lines
D5	high and low voltage	equipment and power lines
D6	high and low voltage	equipment
D7	very high voltage	power lines
D8	high voltage	transformers
D9	very high voltage	transformers
D10	very high and high voltage	electrical substations
D11	very high voltage	power lines
D12	high voltage	power lines

Table 2.1: The short description of the datasets analysed in this study

For the purpose of this study, we thus relied on the measurements of the geomagnetic field. We used the data from the nearest measuring station, the Geomagnetic Observatory Budkov in Šumava mountains, operated by the Geophysical Institute of the Czech Academy of Science. They produce minute measurements of the full vector of the induction of the geomagnetic field. The measurements of the geomagnetic field were downloaded from the Intermagnet[1] data archive, the gaps in the measurements (only 180 minutes over more than 13 years) were filled by using the measurements from Chambon-la-Forêt station in France to have an uninterrupted data series.

From these measurements, we constructed a K index, which is typical for characterizing the level of geomagnetic activity in similar applications. The K index was calculated in a standard way using the value of 3-hour maximal deviations, with a limit of 500 nT for $K = 9$. To obtain daily values that could be compared with the failure rate with daily granularity we averaged 3-hour K indices in each day. We realise that it may not be wise to average the semilogarithmic quantity, but as we will show later, we are not using the absolute values of K index as a reference, but rather its evolution in time.

Minute measurements of the geomagnetic field served as an input data for modelling the geoelectric field during the days of increased geomagnetic activity in the Czech Republic and for estimation of voltages which are induced in the transmission network or conductive structures. Since we did not dispose with more information about the network itself, e.g., admittance and earthing impedance matrices or direction of the power lines, we were not able to calculate GICs in transmission network in the Czech Republic. However, induced geocurrents calculated from our model of geoelectric field served as a good estimate for the GICs in such a region.

[1] http://www.intermagnet.org/

3. Methodology

Only recently, research has been focused on the long-term impact of fluctuating solar activity on the network infrastructures. Schrijver and Mitchell [2013] studied the disturbances in the US electric power grid for the period from 1992 to 2010. They found, with more than 3σ significance, that approximately 4% of the disturbances in the US power grid are attributable to strong geomagnetic activity and associated GICs. This study was followed by Schrijver et al. [2014], where the insurance claims due to the disturbances in the electric power grid were studied. It turns out that in 5% of days with elevated geomagnetic activity, the number of claims is an increase by approximately 20% . The authors concluded that there are 500 claims per year directly associated with the operation of the US grid caused by solar activity.

To our knowledge, a single study was published dealing with GICs in the Czech Republic. Hejda and Bochníček [2005] analysed the pipe-to-soil voltages measured in oil pipelines in the Czech Republic during the Halloween storms in 2003 and showed that the simplest plane wave and uniform Earth-model of the electric field corresponded well to the measured pipe-to-soil voltages. To complete the picture, the study performed in a neighbouring country must be noted. Bailey et al. [2017] modelled and measured the GICs on the Austrian electric power grid. They demonstrated that the Austrian power grid is susceptible to large GICs in the range of tens of Amperes, particularly from strong geomagnetic variations in the east–west direction. That is due to the low surface conductivity in the region of the Alps.

3.1 Inspiration

The main source of information about the methodology was a study done by Schrijver and Mitchell focused on disturbances in the US electric grid associated with geomagnetic activity [Schrijver and Mitchell, 2013]. Secondary we used paper published by Schrijver et al. [2014], where they statistically analysed 11 242 insurance claims from 2000 to 2010 for equipment losses and related business interruptions in North American commercial organizations that are connected to damage or disturbance of electronic equipment.

As stated in Schrijver and Mitchell [2013] eruptive events eventually trigger disturbances in the geomagnetic field which in turn give rise to GIC in conductive layer and infrastructure of the Earth and causes disturbances in the electrical power grid. The magnitude of the GIC depends on several factors:

- properties of the solar wind,
- location and time of the day,
- structure of the Earth's magnetic field,
- conductivity of the Earth,
- architecture of the electric power grid.

They used retrospective cohort analysis to quantify the impact of geomagnetic activity on the North American electricity network for 19 years. It turned out that with more than 3 σ significance, 4% of all disturbances reported in the US power grid, can be attributed to strong geomagnetic activity and GICs. They worked with 1 216 reported failures out of which some disturbances are attributed to weather conditions, operator and equipment failures, vandalism, an act of sabotage etc.

The methodology which they applied is similar to the one used in epidemiological method studies. Schrijver and Mitchell analysed the list of disturbances from 1992 to 2010 obtained from North American Electric Reliability Corporation (NERC, data from 1992) and Energy Reliability of the Department of Energy (DOE, data from 2000) that are published annually and covered 340 000 km of high-voltage transmission lines linking 1 000 power plants within the US. Together 1 216 reported disturbances in NERD-DOE reports group various causes of weather conditions (storm, lightning etc.), operator faults, equipment or transmission failure and so on. There is a growing trend of disturbances frequency in time. However, no clear correlation between solar flares and disturbances in power grid was found but this was not even expected. There are a lot of factors affecting the coupling of the GIC into the transmission network through the structure of the geomagnetic field to the structure of the transmission network itself.

Lack of detailed information about weather condition, electric network and connection between disturbances reported in NERC and DOE led to the more problematic selection of input data. It was difficult to decide whether an event such as lightning or component failure are related to solar activity and so they had to be removed from the list of disturbances. Nevertheless, it may well be that the grid disturbance ensue only because other factors, possibly including space weather, put the system in a state of increased susceptibility. Selection of disturbances is based on criteria including space weather effect. Only disturbances which can be excluded a priori are planned maintenance or fuel shortages. Also, operator error was not removed from the list because it was not clear if the operators were responding to changing grid conditions or a local need. Since the number of failures is quite low they decided to work with a complete set of reported grid disturbances and so did not increase biases in the process.

To estimate disturbances in the geomagnetic activity they used different approaches. From the measurement of the minute-by-minute geomagnetic field, they constructed a maximum value of $\frac{\partial B}{\partial t}$ for 30 minutes interval for an average of two stations that are located along central latitudinal axis of the US. They used K_p index to estimate large-scale geomagnetic activity and interaction of the geomagnetic field with the variable solar wind. From NOAA catalogue of solar flares they selected flares of M and X classes (GOES classes) and compared them with the list of disturbances. All of these indices show the same results in terms of disturbances of the grid. In other words, it did not matter which index was used as a description of geomagnetic activity, statistical analysis showed similar behaviour for all of them.

Since the electric grid is variable in time and so operating procedures they decided to use a method which compares grid disturbances frequency for days with elevated geomagnetic activity with control sample for a day with lower geomagnetic activity while all other conditions stay the same. They worked

with two control samples with same frequencies chosen near to dates of high exposure. All of the background conditions (weather, fuel price and vandalism) not connected to a condition in geospace were changing independently from space weather.

Basically, they compared frequencies of grid disturbances under severe space weather conditions with those under light space weather conditions, with the grid in otherwise similar conditions. Averaged grid disturbances g_a for days of top $p = 2, 5$ and 10 percentile of geomagnetic activity were compared with disturbances rate in the absence of strong geomagnetic activity. Using 50 day intervals centred on days with high $\frac{\partial B}{\partial t}$ they ensured statistically comparable state of the electric grid. They selected a random date within this 50 day window but more than 5 days away from the reference dates. Corresponding disturbance rate g_r contains days with high geomagnetic activity as well as days of no significant activity. Second control sample included dates for the last 3 day intervals of the lowest $\frac{\partial B}{\partial t}$ within 50 day intervals, yields the disturbance rates g_i. For percentile levels $p = 2, 5, 10$ the inequality $g_a > g_r > g_i$ held which means the highest disturbance frequency was during geomagnetic active days, lower for randomly selected days and the lowest when geomagnetic activity was lowest. They found that at least 50 disturbances were attributable to enhanced geomagnetic activity during 19 year period of their study.

They repeated the study but instead of $\frac{\partial B}{\partial t}$ they used K_p index. Analysing daily averaged K_p they found statistically consistent results with those mentioned above using $\frac{\partial B}{\partial t}$ to describe the level of the geomagnetic activity.

Finally, they compared the disturbance database with solar flare catalogue obtained from NOAA and select the largest M and X flares. Since 1992 to 2010, 1879 M and 1054 X class flares were recorded. Almost half of M class flares and more than 90% of X class flares were accompanied with CME. They determined disturbance frequency $f_{a,i,r}$ using three criteria:

1. f_a for the $2 - 5$ day intervals after large solar flare

2. f_r for the 4 day intervals randomly selected within 50 day of major solar flare

3. f_i for the first 4 day intervals before the selected solar flare that end 7 day interval of no major solar flare (relative quiescent condition)

They found a significant increase of reported disturbances in days after major flaring relative to a quiescent interval, at the significance of about 4.5σ but no significance between f_r and f_a. Choosing days with at least one X class flare this significant between f_r and f_a increase to 2σ. For dates with more than one flare, there was even more pronounced difference but with higher uncertainties. 50 disturbances out of all disturbances were attributed to solar activity.

It turned out that the susceptibility of the US power grid is statistically similar to geomagnetic activity for both classes of cause, the one contained clear attributions to weather (wind, ice, lightning), external factors (fire, earthquake, sabotage), technical issues (maintenance) and other complementary list contained line errors, voltage reduction and so on. This hold for all three indices of geomagnetic and solar activity.

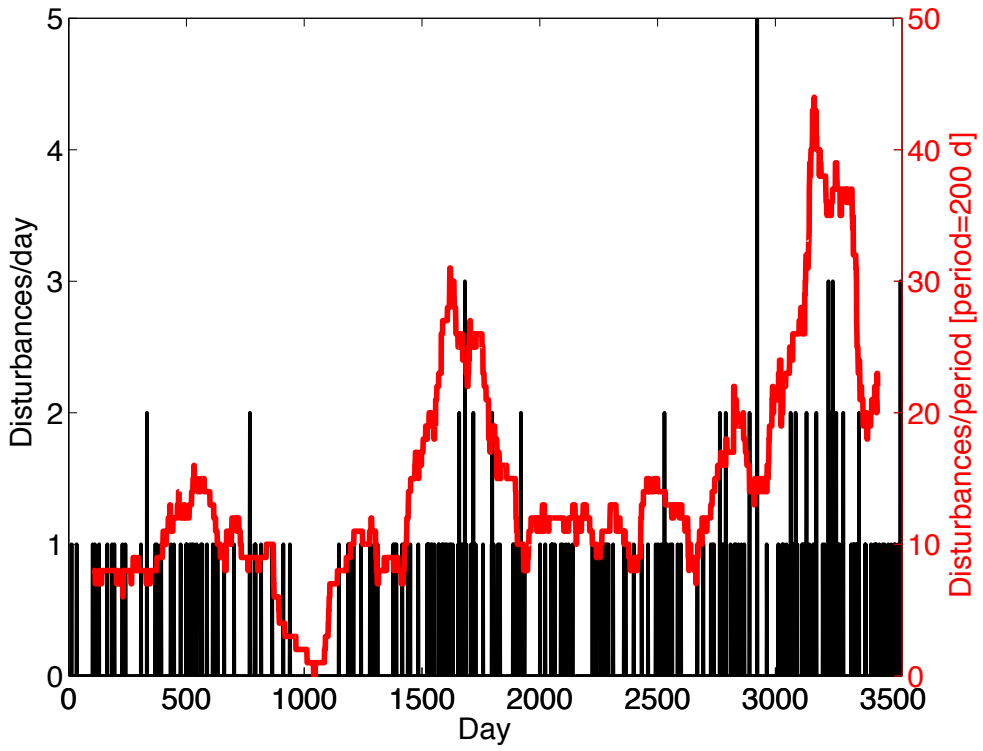

Figure 3.1: Number of disturbances occurring in a day (black) for distributor D1. Most of the time there is one failure per day, there are days without any or sometimes even more than two failures. Due to the character of the curve, we redraw binated version of the curve (red) with a floating 200-day window from which we can see secular trend.

To sum it up, they found a statistically significant enhancement in the frequency of power grid disturbances in days of increased geomagnetic activity, regardless of which measure for the geomagnetic activity they used. This enhancement means that at least 4% of all disturbances were attributed to enhanced geomagnetic activity. Although this result is significant the number is relatively small in comparison with the number of all reported disturbances.

3.2 Data

We are looking for a relationship between the increased geomagnetic activity represented by K index and disturbances in the Czech power grid. As an example, we demonstarte how failure log data look in the Figure 3.1

3.2.1 Analysis of list of disturbances

At first, we investigate the failure rates in the Czech power grid and search for the correlation with increased solar activity. By means of statistical methods, we compare the appearance of the failures in periods of increased geomagnetic activity with periods of decreased activity.

The first distributor reported 252 (240 after sorting) failures from 2006 to 2015 see Figure 3.1.

Second distributor operated with 906 (789 after sorting) registered disturbances on very high voltage transmission since 2007 to 2017, 523 (522 after sorting) disturbances registered on high voltage transmission from 2012 to 2017 and for the same period there were 100 disturbances (91 after sorting) on low voltage transmission lines.

We obtained 863 disturbances registered during the years 2011 to 2016 from the third distributor. After exclusion, those that could not be apparently caused by increased geomagnetic activity 357 disturbances left since there were lot of reported disturbances without the date when they occurred or those without the indicating number. We sorted these data into three categories according to their failure location:

- transformers
- transmision lines
- the rest

The last distributor provided a report of disturbances from 2008 to 2017. We divided them into 6 categories according to the disturbance location:

- high voltage to low voltage transformers (383 reported disturbances)
- very high voltage to high voltage transformers (3 724 reported disturbances)
- transmission lines of low voltage (366 247 reported disturbances)
- transmission lines of high voltage (46 277 reported disturbances)
- transmission lines of ultra high voltage (1 716 reported disturbances)
- stations (56 643 reported disturbances)

3.2.2 Analysis of K index

From fluctuations of horizontal components of the geomagnetic field measured at Budkov station, K index may be calculated (see Table 1.1). Comparison of self computed K index with K index for another nearby station in Moscow showed a good agreement. We found an increase of K index values during dates of polar lights comparing them with days when aurora was observed.

The K index describes the fluctuations of the geomagnetic field that responds to changes in solar activity. These changes also include phenomena related to the 28-day period of Sun rotation and also the annual period connected to the interplanetary magnetic field. Despite the fact that randomly eruptive events have the greatest impact on the Earth we worked with unfiltered to indexes that describe the overall geomagnetic activity that we are interested in.

3.3 Methodology of our study

The correlation coefficient between the K index and the failure rate of all series is practically zero as expected. The power-grid disturbances are not expected to occur immediately after the exposure to the increased geomagnetic activity. For a stringent example we need to note that in the case of the failure of the step-up transformer at Salem 2 generator station in 1989, the damage was discovered during a routine test a week after the exposure to large-amplitude GICs [NERC, 1990]. Yet, the device was written off. During 25 months after the storm in March 1989, multiple key transformers collapsed with a variety of delays after the exposure. Thus there is a time delay expected with an unknown value, which depends on many conditions of the activity and on the device itself. E.g. for the Greek power grid Zois [2013], found the delay to be up to several years. The close-to-zero correlation was found also by Schrijver and Mitchell [2013] in a study principally similar to our.

We used a different approach and compared the number of failures recorded by Czech distributors in the period of increased geomagnetic activity with the number of failures during the period of low geomagnetic activity and with a randomly selected period. The lengths W and number n_i of these three types of the interval were chosen in the same way in order to have all other conditions similar. The length W is a free parameter which ranges between 10 and 200 days serve as accumulation windows for the series of power-grid disturbances. On the other hand, the number of intervals n_i is selected by our code (see 4.4).

Let us have working hypothesis saying that increased geomagnetic activity will be reflected in the number of disturbances recorded on the power grid then the overall number of disturbances N_h during high geomagnetic activity should be larger than the number of disturbances N_l recorded during the period of geomagnetic inactive days. We would expect that the number of failures N_r for randomly selected intervals will be between these two numbers since they can contain days with higher activity as well as days with decreased geomagnetic activity.

Obviously, the results can be affected by the lengths of the considered intervals. However, it is not our aim to focus on choosing the optimal interval length so we evaluated the results for a set of lengths.

4. Statistical methods

Even when some relation holds, its statistical significance must be tested. Using different statistical methods we verify the validity of working hypotheses. We are working with two hypotheses:

- working hypothesis which says that differences between disturbances recorded during geomagnetic active period and geomagnetic inactive period are due to chance,
- alternative hypothesis which says that these differences has a statistical significance.

We cannot decide weather the hypothesis is valid, we can only test its significance and thus say whether this hypothesis needs to be rejected or not. In this manner, we tested the statistical significance of the null hypothesis using binomial test. In case of its rejection alternative hypothesis left and we got an indication of strong dependence of increased failure rates with increased geomagnetic activity.

The control-sample test tell us more about the relative increase of the recorded disturbances during geomagnetic active days compared to geomagnetic inactive days. Lastly, we checked cumulation of disturbances according to exposure of local maximum in geomagnetic activity and so took a look on the causality between the failure rates and increased activity.

4.1 Binomial test

The binomial test is typically used in cases of two expected realizations of the phenomenon. It is suitable also for a relatively small sample.

The binomial test states the probability P that the registered differences between two of N_h, N_l, N_r are in accordance with the model. Our model is the reversed hypothesis, that says there is no difference between the number of failures registered in the periods around local maxima of activity, local minima of activity, and the randomly selected intervals. If P is lower than 5% (our selection of the statistical significance), then we reject the reversed hypothesis. In such a case, we obtained an indication that indeed, there is a statistically significant increase in failure rates after the maximum of the geomagnetic activity. P is computed as

$$P_{\mathrm{h,l}} = 2\sum_{k=x}^{n} \binom{n}{k} p^k (1-p)^{n-k} \tag{4.1}$$

where for testing the pair N_h and N_l, $n = N_\mathrm{h} + N_\mathrm{l}$ denotes the total number of failures in two sets of chosen intervals. The parameter p states the model-expected probability of the disturbance occurring during the high-activity intervals. In the tested (that is in the reversed) hypothesis we assume that the probability of the disturbance occurring during the maximum or the minimum be the same, i.e. $p = 1/2$. Finally, $x = \max(N_\mathrm{h}, N_\mathrm{l})$. Analogous relations may be written for pairs N_h and N_r and N_r and N_l.

The binomial test is a principal approach in our study to assess the possibility of the disturbance rate to be affected by the geomagnetic activity. It gives us the answer to the question whether it is possible, for the given dataset and the accumulation window W, to register a difference in the failure rates occurring during the minima and maxima of the geomagnetic activity. It gives us a qualitative answer.

4.2 Case control test

To quantify the difference in the failure rates for both different situations (minima and maxima of the geomagnetic activity) we evaluated a relative risk.

The relative risk R is a value coming from the case-control analysis. It is a common quantity in e.g. epidemiological studies or when testing the effectiveness of the vaccination. It uses two samples: the sample which was exposed to a certain causal attribute (those are the testing object with the vaccine) and a control sample which was not exposed. Then the number of positive and negative cases in both samples are compared. We could not use the number of disturbances in the intervals of an increased and decreased geomagnetic activity in the calculation of the relative risk. Thus we constructed a different statistical series. For both intervals around the local maxima of the geomagnetic activity (the sample with the causal attribute), we computed the number of days in which disturbances were registered and the number of days without disturbances. The analogous two numbers were computed for the interval around the local minima (the control sample without the causal attribute). Then we computed the relative risk as

$$R = \frac{a}{a+b} / \frac{c}{c+d}, \tag{4.2}$$

where a is the number of days with failures and b without them, both for intervals with increased solar activity. For intervals with lower solar activity, c is the number of days with failure and d is the number of days without any.

The relative risk is 1 if there is no difference between the two groups differing in the causal attribute. If $R < 1$ then more often positive cases occur in a group without a causal attribute (i.e. contrary to expectation), if $R > 1$ then positive cases occur more often in a causal attribute group.

4.3 Test of disturbances cumulation

The two tests described above may give us an indication of a statistically significant increase in the failure rates in the periods of the increased geomagnetic activity. These tests still do not prove the causal link, the binomial test is an "advanced correlation measure" to some extent.

If the increased failure rates are indeed caused by the increased geomagnetic activity, where a positive but unknown time lag may play a role, one would expect that the failure rates will be larger after the geomagnetic activity maximum than before. Thus we compared the number of disturbances in the intervals of length W immediately before the local maximum with the number of disturbances in the intervals of the same length placed immediately after the maximum. We

compared the mean daily failure rates in the two intervals (we would expect the mean to increase after the local maximum), the relative mean increase in the units of standard deviation of the daily failure rates, and of course we ran a binomial test evaluated by (4.1) to test the statistical significance.

A similar comparison was done for the minima. For the minima, we do not expect a significant change in the failure rate before and after the minimum.

4.4 The code

To perform the statistical analysis outlined above we wrote a series of programs in PYTHON 3.6 that allowed us to study the effects of various parameters in the code on the results. Such an approach also ensured that the processing of all the data files was done in exactly the same way. For the purpose of efficient data processing, we have created an algorithm using standard library, NumPy, SciPy and csv packages. The program had two principal inputs for each run:

1. the series of daily-averaged K index,

2. the series of dates when disturbances on the power grid occurred in the given dataset.

The analysis was executed for a set of window lengths W.

The code first smoothed the series of K indices with a boxcar window with a width of W, so that the time-scales of the two series to be compared were similar. In the smoothed series the code then detected local maxima and minima from the first derivative computed in the Fourier space. The code goes through the series of Fourier derivative and looks for the point where derivative crosses zero. Due to sampling, there are no zero points so we could not use stationary points to find extremes of K index. However, if the value changes from positive to negative or vice-versa it has to pass through zero. At the same time, from derivative sign maximum or minimum can be determined. If the derivative changes from positive to negative it must be the maximum and in the opposite case it is the minimum.

Then the neighbouring minima and maxima were paired together so that their paring minimises the possible effects of the secular development of the power grid that could possibly lead to the trends in the failure rates. On the other hand, the requirement was that the neighbouring minima and maxima do not overlap within W bounds. In such a case the next neighbouring minimum was selected for the maximum. We also ensured that the maximum+minimum pairs were unique.

Around each minimum and maximum, we drew an interval with a total length of W days. The window was positioned such that its centre was placed at the local minimum and its beginning was placed at the local maximum. We performed our tests for a selection of values of W. For each dataset, we had n_i pairs of maxima and minima of geomagnetic activity. Moreover, we randomly selected the same number n_i of intervals of length W. These served as an additional testing sample. An example of the local extreme detection and their pairing for $70, 50$ and 30 day windows are given in Figure 4.1-4.3, a remaining set is then given in Figure A.1-A.7 in the Attachments.

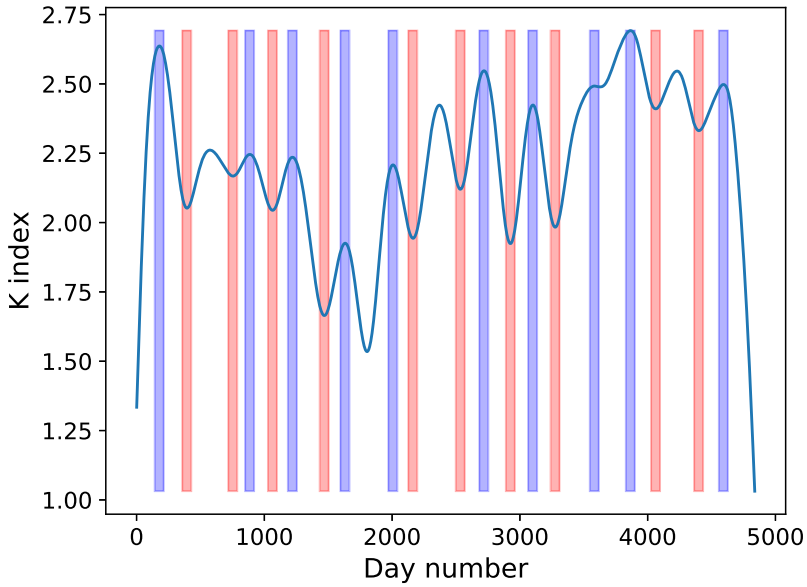

Figure 4.1: Daily averaged K index and the pairing of the local maxima (blue) and neighbouring non-overlapping minima (red) detected by our code for $W = 70$.

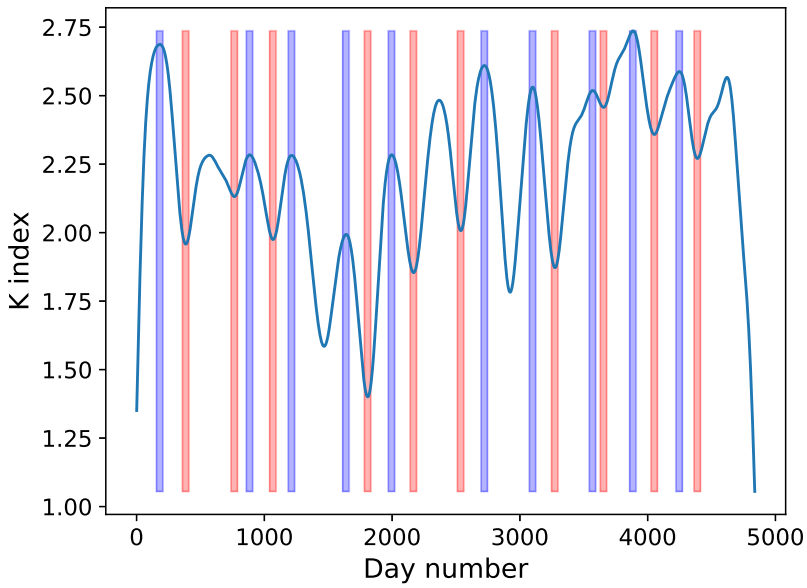

Figure 4.2: Daily averaged K index and the pairing of the local maxima (blue) and neighbouring non-overlapping minima (red) detected by our code for $W = 50$.

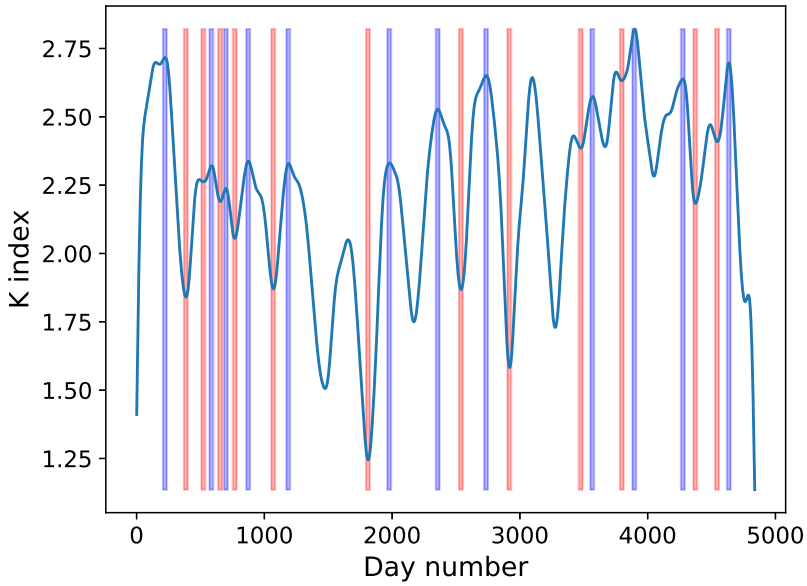

Figure 4.3: Daily averaged K index and the pairing of the local maxima (blue) and neighbouring non-overlapping minima (red) detected by our code for $W = 30$.

In the selected intervals we counted the total number of failures N_{h} falling into the maximum intervals (that is during increased geomagnetic activity), number of failures N_{l} falling into the minimum intervals (that is in the low-activity periods) and number of failures N_{r} falling into the random intervals. We evaluated the probability given by (4.1) and computed the risk given by (4.2). For each maximum and each minimum, the code then evaluated the number of failures falling into the intervals of width W occurring immediately before the maximum (or minimum) and after it. We only remind that these numbers depend on the length W of the accumulation window.

In the case when increased geomagnetic activity on average induces a subsequently larger failure rate of power-grid devices, we would expect the relation

$$N_{\mathrm{h}} \geq N_{\mathrm{r}} \geq N_{\mathrm{l}}. \tag{4.3}$$

4.5 Results

We found that the results depend strongly on the selection of W. Smaller windows increase the noise levels because lesser numbers of disturbances fall into the tested intervals. Also, shallower local minima and/or maxima are present in the series of K index due to the smaller smoothing see Figure (4.4). On the other hand, too large values of W cause the K index series to be overly smoothed and the pairing of the neighbouring minima and maxima gets difficult, because the requirement of the non-overlapping intervals is too strong see Figure (4.5). As a consequence, the "neighbouring" maximum+minimum pairs may be hundreds of days apart. The interpretation of such comparison is then complicated as over a period of hundreds of days the secular trends connected with the network development or

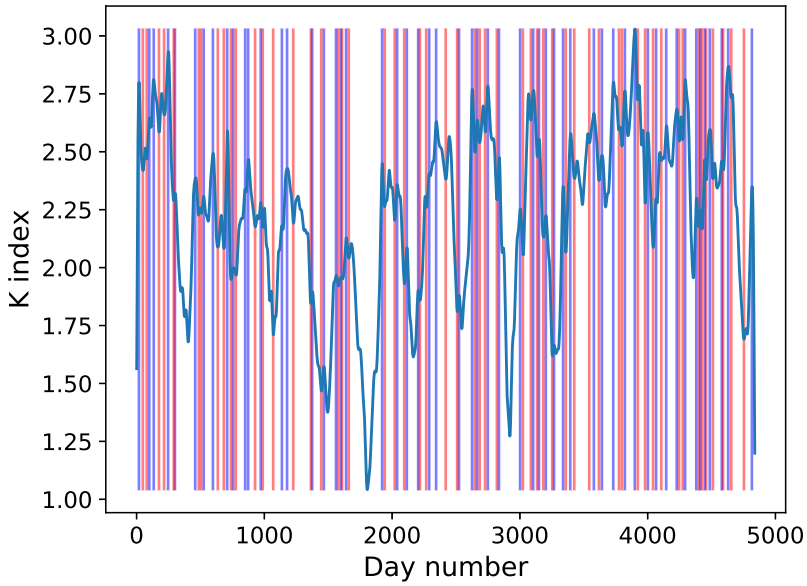

Figure 4.4: Daily averaged K index and the pairing of the local maxima (blue) and neighbouring non-overlapping minima (red) detected by our code for $W = 10$.

seasonal changes increase their importance. In the following, we thus discuss mainly the results obtained for windows $W = (30, 50, 70)$ days.

We found that in most cases the differences in the number of failures in the maxima and minima are not statistically significant. That is also demonstrated in an example Table 4.1 Table 4.2 and Table 4.3. A complete set of tables for all remaining values of W are given in the Table A.1–A.8 in the Attachments.

Only the datasets D10, D11, and D12 seem to indicate a statistically significant increase of N_{h} coherent with the expectations. In those cases also N_{r} lies in between N_{h} and N_{l}, exactly as expected when the geomagnetic activity be an agent influencing the number of failures. These three datasets behave the same for all windows W in the range of 30 to 120 days. Interestingly, these datasets record disturbances on the high-voltage and very-high-voltage power lines and also on electrical substations.

Datasets D1 and D7 show a statistically significant increase of N_{h}, but N_{r} do not concord the expectations. In the case of D1, one could say that the differences between N_{h} and N_{r} is not statistically significant, on the other hand, in the case of D7 N_{r} is far too low to be explained by chance. We note that D1 aggregates disturbances on the equipment of the spinal transmission network, whereas D7 logs disturbances on the high-voltage power lines. Both D1 and D7 often show similar behaviour for different values of W.

Differences registered in the remaining datasets are not statistically significant.

The relative risk as we defined it turned out to be not very useful in the analysis we performed. The R value is meaningless when the number of recorded disturbances is low due to the statistical significance of R. On the other hand, when the number of disturbances is large, as in e.g. D12, the $R = 1$ by definition. Due to the daily granularity of the failure logs, in such a case there always is at least one disturbance each day in which the data exist. Then obviously the R

Dataset ID	Intervals	N_{h}	N_{r}	N_{l}	$P_{\mathrm{h,l}}$	$P_{\mathrm{r,l}}$	$P_{\mathrm{h,r}}$	a	b	c	d	R	I_{r}
D1	7	46	23	22	0.0049	0.00762	1.0	46	444	22	468	2.09091	0.07
D2	4	74	57	62	0.34559	0.16188	0.71403	74	206	62	218	1.19355	–
D3	4	8	9	13	0.38331	1.0	0.52347	8	272	13	267	0.61538	–
D4	4	13	17	22	0.17547	0.58466	0.5224	13	267	22	258	0.59091	–
D5	4	32	48	33	1.0	0.09291	0.11927	32	248	33	247	0.9697	–
D6	4	19	19	12	0.28104	1.0	0.28104	19	261	12	268	1.58333	–
D7	8	84	9	31	$< 10^{-5}$	$< 10^{-5}$	0.00068	84	476	31	529	2.70968	0.53
D8	7	541	520	484	0.08022	0.53923	0.26933	298	192	279	211	1.0681	–
D9	7	46	50	57	0.32448	0.75965	0.56209	44	446	51	439	0.86275	–
D10	7	8661	7493	7317	$< 10^{-5}$	$< 10^{-5}$	0.15043	490	0	490	0	1.0	0.13
D11	7	285	149	120	$< 10^{-5}$	$< 10^{-5}$	0.0876	194	296	92	398	2.1087	0.74
D12	7	7073	6080	5543	$< 10^{-5}$	$< 10^{-5}$	$< 10^{-5}$	489	1	489	1	1.0	0.22

Table 4.1: Statistical analysis of disturbances in the Czech distribution network for the 70-day window. For datasets D1–D12 we give the number of interval pairs, the total number of reported disturbances in the periods of increased activity, decreased activity, and in the random intervals. Then we give the probabilities P with which the differences in the number of failures between two intervals are due to chance. In the last section we give necessary values for the computation of the relative risk R, and also the value of I_{r}.

Dataset ID	Intervals	N_{h}	N_{r}	N_{l}	$P_{\mathrm{h,l}}$	$P_{\mathrm{r,l}}$	$P_{\mathrm{h,r}}$	a	b	c	d	R	I_{r}
D1	7	34	24	16	0.01535	0.23705	0.26819	34	316	16	334	2.125	< 0.01
D2	4	53	36	42	0.30489	0.08932	0.57159	53	147	42	158	1.2619	–
D3	4	7	5	11	0.48068	0.77441	0.21011	7	193	11	189	0.63636	–
D4	4	10	16	13	0.67764	0.32694	0.71107	10	190	13	187	0.76923	–
D5	4	27	24	21	0.47088	0.77977	0.76599	27	173	21	179	1.28571	–
D6	4	17	8	10	0.24779	0.10775	0.81453	17	183	10	190	1.7	–
D7	9	89	4	31	$< 10^{-5}$	$< 10^{-5}$	$< 10^{-5}$	89	361	31	419	2.87097	0.62
D8	7	405	331	373	0.26638	0.00709	0.12223	228	122	199	151	1.14573	–
D9	7	33	35	39	0.556	0.9036	0.72755	31	319	33	317	0.93939	–
D10	7	6239	5858	5230	$< 10^{-5}$	0.00055	$< 10^{-5}$	350	0	350	0	1.0	0.13
D11	7	203	195	85	$< 10^{-5}$	0.72573	$< 10^{-5}$	140	210	69	281	2.02899	0.65
D12	7	5035	4637	3990	$< 10^{-5}$	5e-05	$< 10^{-5}$	349	1	349	1	1.0	0.19

Table 4.2: Statistical analysis of disturbances in the Czech distribution network for the 50-day window. For datasets D1–D12 we give the number of interval pairs, the total number of reported disturbances in the periods of increased activity, decreased activity, and in the random intervals. Then we give the probabilities P with which the differences in the number of failures between two intervals are due to chance. In the last section we give necessary values for the computation of the relative risk R, and also the value of I_{r}.

Dataset ID	Intervals	N_{h}	N_{r}	N_{l}	$P_{\mathrm{h,l}}$	$P_{\mathrm{r,l}}$	$P_{\mathrm{h,r}}$	a	b	c	d	R	I_{r}
D1	9	17	18	13	0.58466	1.0	0.47313	17	253	13	257	1.30769	–
D2	5	24	41	37	0.12373	0.04635	0.73434	24	126	37	113	0.64865	–
D3	5	7	4	7	1.0	0.54883	0.54883	7	143	7	143	1.0	–
D4	4	9	17	11	0.8238	0.16864	0.34493	9	111	11	109	0.81818	–
D5	4	16	16	15	1.0	1.0	1.0	16	104	15	105	1.06667	–
D6	4	7	10	5	0.77441	0.62906	0.30176	7	113	5	115	1.4	–
D7	9	44	4	46	0.91613	$< 10^{-5}$	$< 10^{-5}$	44	226	46	224	0.95652	–
D8	7	197	198	211	0.51989	1.0	0.55299	126	84	125	85	1.008	–
D9	7	27	18	24	0.77977	0.23269	0.4408	24	186	22	188	1.09091	–
D10	7	3580	3514	3377	0.01544	0.44027	0.10135	210	0	210	0	1.0	< 0.01
D11	7	110	101	89	0.15609	0.58191	0.42493	74	136	65	145	1.13846	–
D12	7	2975	2329	2662	3e-05	$< 10^{-5}$	$< 10^{-5}$	209	1	210	0	0.99524	0.04

Table 4.3: Statistical analysis of disturbances in the Czech distribution network for the 30-day window. For datasets D1–D12 we give the number of interval pairs, the total number of reported disturbances in the periods of increased activity, decreased activity, and in the random intervals. Then we give the probabilities P with which the differences in the number of failures between two intervals are due to chance. In the last section we give necessary values for the computation of the relative risk R, and also the value of I_{r}.

Dataset ID	$\mu_{-\max}$	$\mu_{\max+}$	$\sigma_{-\max}$	$\sigma_{\max+}$	$\mu_{-\min}$	$\mu_{\min+}$	$\sigma_{-\min}$	$\sigma_{\min+}$	$\frac{I_{\max}}{\sigma_{-\max}}$	$\frac{I_{\min}}{\sigma_{-\min}}$	P_{-+}
D1	0.44	0.66	0.62	0.79	0.34	0.29	0.61	0.51	0.343	-0.094	0.03355
D2	1.06	1.06	0.77	0.79	0.77	0.71	0.72	0.83	0.0	-0.079	0.42219
D3	0.11	0.11	0.32	0.32	0.16	0.11	0.36	0.32	0.0	-0.118	0.75391
D4	0.49	0.19	0.58	0.42	0.29	0.33	0.54	0.53	-0.518	0.08	0.34493
D5	0.79	0.46	0.69	0.65	0.59	0.43	0.71	0.6	-0.473	-0.222	1.0
D6	0.33	0.27	0.47	0.53	0.34	0.11	0.58	0.32	-0.122	-0.392	0.15159
D7	1.1	1.2	0.93	0.82	0.43	0.39	0.55	0.54	0.108	-0.078	0.51041
D8	6.6	7.73	2.85	3.62	7.61	6.49	3.5	2.56	0.396	-0.323	0.00002
D9	0.71	0.66	0.94	0.89	0.7	0.6	0.82	0.85	-0.061	-0.122	0.00109
D10	112.99	123.73	21.08	21.2	101.09	103.49	19.34	20.01	0.51	0.124	0.00073
D11	4.29	4.07	3.06	2.23	1.44	2.13	1.31	1.6	-0.07	0.525	0.81275
D12	87.87	101.04	19.02	20.4	82.93	76.57	20.31	20.11	0.692	-0.313	$< 10^{-5}$

Table 4.4: Comparison of the failure rates around the local minima and maxima. In the first section we give mean values (μ) and standard deviations (σ) for the intervals of length $W = 70$ days before local maxima (subscript $-\max$) and after the maxima (subscript $\max+$). In the second section analogous parameters are evaluated for local minima. In the third section we give the relative increase of the means in the units of the standard deviation evaluated before the extreme. In the last section we give the probability that the differences in the interval before the maximum and after the maximum are due to chance.

Dataset ID	$\mu_{-\max}$	$\mu_{+\max}$	$\sigma_{-\max}$	$\sigma_{+\max}$	$\mu_{-\min}$	$\mu_{+\min}$	$\sigma_{-\min}$	$\sigma_{+\min}$	$\frac{I_{\max}}{\sigma_{-\max}}$	$\frac{I_{\min}}{\sigma_{-\min}}$	p_{+-}
D1	0.46	0.68	0.57	0.9	0.54	0.3	0.7	0.46	0.384	-0.343	0.83882
D2	1.08	1.06	0.89	0.88	0.66	0.84	0.62	0.67	-0.022	0.29	0.89192
D3	0.12	0.14	0.32	0.35	0.14	0.1	0.35	0.3	0.062	-0.115	0.72656
D4	0.6	0.2	0.6	0.4	0.24	0.32	0.43	0.47	-0.667	0.187	0.03516
D5	0.9	0.54	0.7	0.67	0.48	0.38	0.54	0.52	-0.514	-0.186	0.40503
D6	0.32	0.34	0.58	0.62	0.28	0.08	0.49	0.27	0.034	-0.407	0.66362
D7	1.74	1.78	0.98	0.97	0.58	0.54	0.78	0.75	0.041	-0.051	0.91704
D8	6.76	8.1	3.06	2.82	6.86	6.62	2.93	3.47	0.438	-0.082	0.01284
D9	0.76	0.66	0.91	0.97	0.72	0.72	0.85	0.92	-0.11	0.0	0.07076
D10	120.66	124.78	18.85	21.98	96.22	105.52	18.36	20.32	0.219	0.506	0.79098
D11	4.24	4.06	2.59	2.63	1.4	1.76	1.06	1.61	-0.07	0.34	0.51391
D12	96.1	100.7	20.8	22.07	78.48	78.3	18.55	22.14	0.221	-0.01	0.6996

Table 4.5: Comparison of the failure rates around the local minima and maxima. In the first section we give mean values (μ) and standard deviations (σ) for the intervals of length $W = 50$ days before local maxima (subscript $-\max$) and after the maxima (subscript $\max+$). In the second section analogous parameters are evaluated for local minima. In the third section we give the relative increase of the means in the units of the standard deviation evaluated before the extreme. In the last section we give the probability that the differences in the interval before the maximum and after the maximum are due to chance.

Dataset ID	$\mu_{-\max}$	$\mu_{+\max}$	$\sigma_{-\max}$	$\sigma_{+\max}$	$\mu_{-\min}$	$\mu_{+\min}$	$\sigma_{-\min}$	$\sigma_{+\min}$	$\frac{I_{\max}}{\sigma_{-\max}}$	$\frac{I_{\min}}{\sigma_{-\min}}$	p_{+-}
D1	0.47	0.57	0.72	0.76	0.47	0.43	0.62	0.67	0.139	-0.054	1.0
D2	1.17	0.8	0.78	0.7	0.93	1.3	0.81	0.9	-0.471	0.451	0.59661
D3	0.27	0.23	0.44	0.42	0.17	0.37	0.37	0.6	-0.075	0.537	1.0
D4	0.37	0.3	0.6	0.46	0.23	0.37	0.5	0.55	-0.11	0.269	0.75391
D5	0.83	0.53	0.86	0.67	0.37	0.47	0.6	0.56	-0.349	0.165	0.83181
D6	0.5	0.23	0.56	0.5	0.13	0.13	0.34	0.34	-0.474	0.0	0.3877
D7	2.1	1.47	1.37	1.09	1.53	1.73	1.06	0.96	-0.461	0.189	0.09246
D8	8.37	6.57	3.12	3.57	7.3	6.7	2.95	3.11	-0.576	-0.204	0.43185
D9	0.47	0.9	0.56	1.01	0.87	1.27	0.88	1.18	0.771	0.452	0.16707
D10	118.3	119.33	28.46	22.5	103.27	111.53	17.15	18.83	0.036	0.482	0.40047
D11	3.9	3.67	2.12	2.45	3.17	2.93	2.15	1.86	-0.11	-0.109	0.93016
D12	91.6	99.17	24.49	35.91	89.1	92.73	19.82	24.6	0.309	0.183	0.0

Table 4.6: Comparison of the failure rates around the local minima and maxima. In the first section we give mean values (μ) and standard deviations (σ) for the intervals of length $W = 30$ days before local maxima (subscript $-\max$) and after the maxima (subscript $\max+$). In the second section analogous parameters are evaluated for local minima. In the third section we give the relative increase of the means in the units of the standard deviation evaluated before the extreme. In the last section we give the probability that the differences in the interval before the maximum and after the maximum are due to chance.

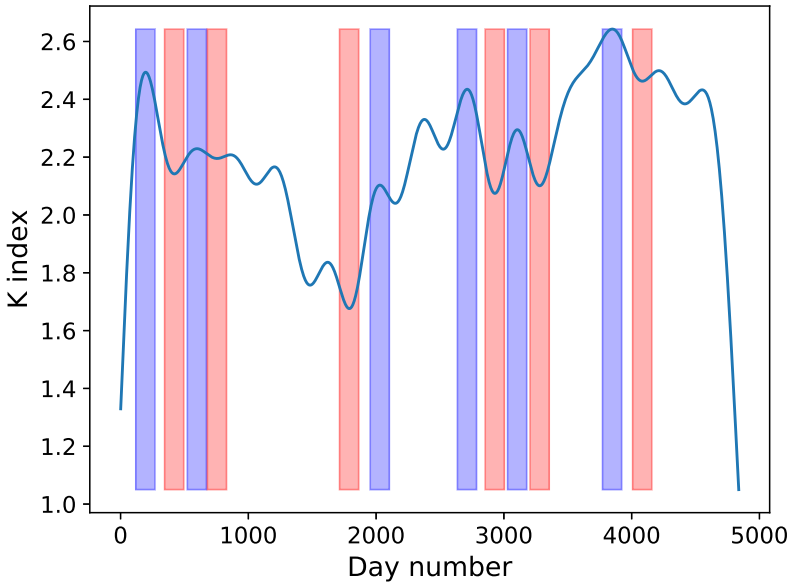

Figure 4.5: Daily averaged K index and the pairing of the local maxima (blue) and neighbouring non-overlapping minima (red) detected by our code for $W = 150$.

is meaningless again. Thus it is useful only in the case when the total number of registered disturbance events is between say 100 and 300. We cannot increase the granularity in time of the populated datasets, thus we cannot choose another suitable parameter to be tested to compute the relative risk. One option would be to split the populated datasets in more datasets e.g. grouped by the geographical location or another criterion. We did not proceed in this way because we do not have confidence in a gain of such a non-trivial manual sorting of the inputs.

Instead, we used a different method to quantify the increase of disturbances in the maxima of geomagnetic activity. For each dataset with positive indication of the increase ($P_{\mathrm{h,l}} < 0.05$) we searched for N_{h1} while keeping N_{l} constant for which $P_{\mathrm{h1,l}} \simeq 0.01$. This would be the boundary value, where we could not reject the hypothesis that the differences are due to change with 1% significance level. Note that for this task we chose a stronger limit of the statistical significance level. The relative increase with a statistical significance would be defined as

$$I_{\mathrm{r}} = (N_{\mathrm{h}} - N_{\mathrm{h1}})/N_{\mathrm{h1}}. \tag{4.4}$$

The values of I_{r} are also given in Table 4.1-4.3 and the supplementary Table A.1–A.8 in the Attachments. In the case of D1, D7, D10, D11, and D12 I_{r} is between 7 and 70 per cent.

We note that the intervals of length W were always centred on the local minimum or on the selected random date, whereas they were placed *after* the local maximum. The motivation was that we expect some delay in the occurrence of the disturbance after the exposure to larger GICs. To test how important this selection is for the results we ran our codes again when centring the intervals on the dates of maxima of geomagnetic activity. The results did not change significantly.

On the other hand, it is worth testing whether the failure rate increases after the maximum of geomagnetic activity. Such a test was achieved by comparing the number of failures and their statistical properties in a window of length W before the maximum with the window of the same length after the maximum. For all of them we computed their mean values (μ). We determined the standard deviations (σ) for the minima. This values were used as a determination whether the failure rate is larger before the local maxima in geomagnetic activity or rather after it. The results are compatible with our hypothesis if there is an increase in the mean daily failure rate after the local maxima and there is more-or-less no change around the local minima. Example results again for $W = 70$ 50 and 30 day intervals are shown in Table 4.4, Table 4.5and Table 4.6 respectively. As a comparison, we derived the same parameters for the local minima. A set of tables for all remaining values of W are given in the Table A.9–A.16 in the Attachments.

The statistical significance of the recorded differences before and after local maxima of geomagnetic activity is low for most of the datasets. Curiously enough, the differences with larger statistical significance are present in the case of datasets D1, D10, and D12, where also the significant difference between N_{h} and N_{l} was found. In those datasets, we observe an average increase of the failure rates by (0.3–0.7)σ (about 10-30% of the daily means) after the maxima, whereas in the control series around the minima we see either a decrease or a much lower increase than in the case of maxima. Furthermore, we record a statistically significant increase around the maxima in dataset D8. This dataset also recorded the differences between N_{h} and N_{l} (see Table 4.1), but the computed probability $P_{\mathrm{h,l}} = 0.08$ was larger than the chosen 5% threshold (the dataset is only 7 disturbances away from the chosen statistical significance threshold). D8 records the disturbances occurring on high-voltage transformers.

5. Geoelectric field

A statistical analysis of the disturbances recorded in the Czech power grid can tell us more about the statistical significance between the increased geomagnetic activity and the failure rates. However, correlation does not mean causality. In this manner, we were looking for the behaviour of the geoelectric field induced in the days with an increased level of geomagnetic activity and from this value we estimated geocurrents induced in two longest transmission lines in the Czech Republic to have a rough estimation about amplitudes of GIC in the Czech transmission network.

Variations of the geomagnetic field are connected to geomagnetic storms which may induce horizontal electric field. Time varying electric field drives GIC in ground-based conductor networks and so have an adverse effects on technological systems such as power transmission grids, oil or gas pipelines, telecommunication cables and railway circuits [Boteler et al., 1998]. In order to studying effects of GIC in conductive structures on the Earth geoelectric field need to be determined at first. This geoelectric field is created by currents and charged particles in the ionosphere and also by currents and charges produced in the conducting Earth.

From the shape of the geomagnetic field (dipole structure), it is clear that the most intense and most frequent geomagnetic storms occur at higher latitudes. However, during major geomagnetic storms, large disturbances can occur even at much lower latitudes (see the section about Historical records of geomagnetic storms). Moreover, the magnitude of GIC in a system depends on several factors:

- topology,
- configuration,
- resistances

of the transmission network. GIC also depends on many technical aspects and varies from one network to another. What can be a hazardous GIC for one grid may be ignored in another. For example, Sweden has experienced harmful GIC effects several times [Pirjola and Boteler, 2006] whereas the neighbouring country, Finland, has never experienced a significant problem due to GIC. Such a surprising variance can be explained by different construction of transformers and transmission grids.

GIC is a product of electromagnetic coupling between space currents and conductors in technological equipment. In general, this problem can be divided into two steps:

1. Determination of the horizontal geoelectric field (geophysical part)
2. Computations of the GIC in the system using Ohm's and Kirchhoff's laws (engineering part)

Since we do not have enough information about resistances and technical parameters of the transmission network in the Czech Republic we focused to the determination of the geoelectric field and further estimation of induced GIC.

5.1 Modelling of the geoelectric field

The determination of the geoelectric field is the same for power networks, railways, pipelines and other conductors. At first, we need to have proper Earth 's conductivity model and knowledge about magnetospheric-ionospheric currents or about the variations of the geomagnetic field. Maxwell's equations

$$\nabla \cdot \mathbf{E} = \frac{\rho}{\epsilon_0}, \tag{5.1}$$

$$\nabla \cdot \mathbf{B} = 0, \tag{5.2}$$

$$\nabla \times \mathbf{E} = -\frac{\partial \mathbf{B}}{\partial t}, \tag{5.3}$$

$$\nabla \times \mathbf{B} = \mu_0 \mathbf{j} + \mu_0 \epsilon_0 \frac{\partial \mathbf{E}}{\partial t} \tag{5.4}$$

connect electric field $\mathbf{E}$ with magnetic field $\mathbf{B}$ and charge density ρ with current density $\mathbf{j}$, μ_0 is vacuum permeability and ϵ_0 is vacuum permitivity. Usually we assume that $\mu = \mu_0$, $\epsilon = \epsilon_0$ and replace charge density $\rho = \rho_{free}$ and current density $\mathbf{j} = \mathbf{j}_{free}$ so we take into account only freely moving charges. All of quantities in (5.1-5.4) are functions of time t and space $\mathbf{r}$.

Maxwell equations have to be accompanied by constitutive equations

$$\mathbf{D} = \epsilon \mathbf{E}, \tag{5.5}$$

$$\mathbf{H} = \frac{\mathbf{B}}{\mu}, \tag{5.6}$$

$$\mathbf{j}_{free} = \sigma \mathbf{E}, \tag{5.7}$$

where the last equation is the Ohm law. Different approaches have been applied to determine the geoelectric field from variations of geomagnetic field, for example, a plane wave method or Complex Image Method [Pirjola and Viljanen, 1998]. For the purpose of our study, we decided to use the plane wave model. Our approach showed a good consistency with a study where Hejda and Bochníček [2005] modelled geomagnetic induced pipe-to-soil voltages in the Czech oil pipelines during the Halloween storm in 2003. The disturbances caused by magnetospheric-ionospheric currents propagate vertically downwards as a plane wave and disturbances caused by geoelectromagnetic variations are described as a wave in this approach.

A common assumption in similar studies of the geoelectric field is that the conductivity of the Earth only varies with depth (1D structure of the Earth). The Earth is replaced by a half-space with a flat surface which is acceptable approximation since GIC is a regional phenomenon. We are using a uniform ground resistivity model which means that the Earth structure is regionally homogeneous with constant conductivity σ. For purposes of this study, we use the value of conductivity $\sigma = 10^{-3}\ \Omega^{-1}$m which is a typical value for Czech territory and it was used also by Hejda and Bochníček [2005]. Assumption of the sufficiently homogeneous geomagnetic field in the whole region of the Czech Republic let us compute geoelectric field only from its variations and so we were not forced to consider ionospheric currents.

What we practically do is:

- we ignore Earth's surface curvature,
- we establish a Cartesian coordinate system where x points northward, y points eastward and z axis points downward,
- we assume plane wave propagation of electric and magnetic field along the z axis,
- we consider the ground as an infinite half-space with a uniform conductivity.

Having an assumption of harmonic time dependence with angular frequency ω then it can be shown that the horizontal geoelectric field component E_y is related to the x component of variation of the geomagnetic field ($\frac{\partial B_x}{\partial t}$) by the equation

$$E_y = -\sqrt{\frac{\omega}{\mu_0 \sigma}} \exp^{i\frac{\pi}{4}} B_x. \tag{5.8}$$

The decrease of the conductivity and the increase of the angular frequency increases the geoelectric field with respect to geomagnetic field.

Time derivative of $B_x(t)$ in Fourier space gives $i\omega B_x$ which can be seen in (5.8). After application of an inverse-Fourier transform we get integro–differential equation coupling electric and magnetic field

$$E_y(t) = -\frac{1}{\sqrt{\pi \mu_0 \sigma}} \int_0^\infty \frac{g(t-u)}{\sqrt{u}} du \tag{5.9}$$

in time domain, where $g(t) = \frac{dB_x(t)}{dt}$. It is in agreement with causality which means that at the time t $E_y(t)$ depends only on the previous values of $g(t)$. Weight of affection by past values decreases with time. A stable solution can be achieved by integration over several hours. The calculation can be done either in time or frequency domain. Correspondingly we can compute $E_x(t)$.

However, the square root in the denominator has a singularity at $t = 0$. This problem is caused due to quasistatic approximation, where displacement currents are ignored. We were dealing with this situation in a way of using a different model of the time evolution of the magnetic field using linear interpolation between discrete data. Details of this method can be found in Love and Swidinsky [2014].

Basically, we need to define time domain of the transfer function $\chi_R(t;\tau)$ which after applying to the magnetic field induces linear changes over time step τ in magnetic field.

$$\chi_R(t;\tau) = \frac{2}{\sqrt{\pi}}[\sqrt{t}H(t) - \sqrt{t-\tau}H(t-\tau)], \tag{5.10}$$

where $H(t)$ is the Heaviside function.

We were modelling the geoelectric field from variations of the geomagnetic field, so we used the same data from which K index was computed (one-minute measurements of geomagnetic field vector). Since we approximated the Earth's surface as an infinite half-space we are interested only into x and y components of the measured geomagnetic field. For more detailed information see Section 3.2. The time derivative of $\mathbf{B}$ can be computed as

$$\frac{\Delta \mathbf{B}(t_j)}{\tau} = \frac{\Delta \mathbf{B}(t_{j+1}) - \mathbf{B}(t_j)}{\tau} \tag{5.11}$$

where $\tau = 60$ s in our case. From discrete values of $\mathbf{B}$ induced electric field can be obtained by convolution with the transfer function (5.10)

$$\mathbf{CE}(t_i;\sigma) = \frac{1}{\sqrt{\mu\sigma}}(\chi_R * \frac{\Delta\mathbf{B}}{\tau})(t_j) \tag{5.12}$$

or explicitly

$$\mathbf{CE}(t_i;\sigma) = \frac{1}{\sqrt{\mu\sigma}}\sum_{j=1}^{i}\chi_R(t_i - t_j)\frac{\Delta\mathbf{B}}{\tau}(t_j) \tag{5.13}$$

where

$$\mathbf{C} = \begin{bmatrix} 0 & -1 \\ 1 & 0 \end{bmatrix}$$

and $\mathbf{C}$ is a spin matrix coming from the curl operator. Due to the plane wave approximation $\mathbf{C}$ has only two dimension.

Finally, we got the equation which does not have a singularity at $t = 0$ and it is straightforward how to use it with measurements of the geomagnetic field. Again, we wrote a program in PYTHON that allowed us to do the numerical computation of (5.13).

5.2 Estimation of induced currents

First, we give a brief introduction to the calculation of GIC in power networks. Unfortunately, we did not operate with technological information necessary for estimation of the GIC but we made some assumptions and estimate currents induced on the conductive transmission lines [Pirjola, 2000].

We can imagine power transmission network as a discrete system with $\mathbf{N}$ earthed nodes which represent transformer substations and they are earthed by the resistances R_{ij}. Then we can calculate GIC as

$$\mathbf{I} = (\mathbf{1} + \mathbf{YZ})^{-1}\mathbf{J}, \tag{5.14}$$

where $\mathbf{Z}$ is the earthing impedance matrix, $\mathbf{Y}$ is the network admittance matrix and unit matrix is $\mathbf{1}$. If we consider that the horizontal component of the geoelectric field $\mathbf{E}$ affect the network then GIC is induced and vector $\mathbf{I}$ represents earthing GIC which flow between the Earth and the conductive network. Positive currents denotes current from the network to the Earth and negative current from the Earth to the network.

The elements $J_i (i = 1, ..., N)$ of the column matrix $\mathbf{J}$ are defined by

$$J_i = \sum_{k \neq i}\frac{V_{ki}}{R_{ki}} \tag{5.15}$$

where V_{ki} is the geovoltage produced by horizontal geoelectric field $\mathbf{E}$ along the path between station i and k. It is defined as a line integral of $\mathbf{E}$ along the power line from point k to point i

$$V_{ki} = \int_k^i \mathbf{E}\cdot d\mathbf{s} \tag{5.16}$$

d**s** is an oriented element along the line.

Admittance matrix **Y** is defined by relation

$$Y_{ij} = -\frac{1}{R_{ij}}, (i \neq j) \tag{5.17}$$

$$Y_{ij} = \sum_{k \neq i} \frac{1}{R_{ij}}, (i = j) \tag{5.18}$$

where R_{ij} is the resistance between i and j nodes.

When we know all of these parameters I_{ik} can be computed as

$$I_{ij} = \frac{V_{ij}}{R_{ij}} + \frac{(\mathbf{ZI})_i - (\mathbf{ZI})_j}{R_{ij}}. \tag{5.19}$$

As it was mentioned above, we do not have any of these matrices which describe features of the network. Since we do not know the exact direction of transmission lines we can make a rough guess of its direction using maps. From the website [1] we chose two longest power transmission lines and found their lengths and resistances

- V413, approximated as a transmission line in the west–east direction only, with a length of 284 km and a specific resistance of 0.0289 $\Omega\,\mathrm{km}^{-1}$.
- V475, approximated as a transmission line in the north–south direction only, with a length of 138 km and a specific resistance of 0.0211 $\Omega\,\mathrm{km}^{-1}$.

First, we estimate the induced voltage using equation (5.16) where the integral is taken along the line i.e., along the path of the transmission line.

Afterwards, we calculated the induced currents induced on this line as

$$\mathbf{J} = \frac{\mathbf{V}}{\mathbf{R}} \tag{5.20}$$

where **V** is our computed voltage and **R** is the resistance of the transmission line. Current **J** corresponds to "perfect-earthing" induced currents, that is **J** would equal to GIC flowing from/to the Earth to the power lines when the earthing resistivity is zero.

5.3 Results

We concentrated mostly on the periods around the maxima of geoelectric field so for each such an event we took the maximum value of **E** or a characteristic value of its variation. From this values we calculated **V** and **J** for both approximated lines.

To ensure that we chose the largest geomagnetic events we went through the website [2] and searched for dates when aurora was observed in the Czech Republic. Aurora can be considered as the strongest manifestation of an increased geomagnetic activity and together with GIC they are the only manifestation of

[1] https://www.oenergetice.cz/

[2] http://www.ukazy.astro.cz/

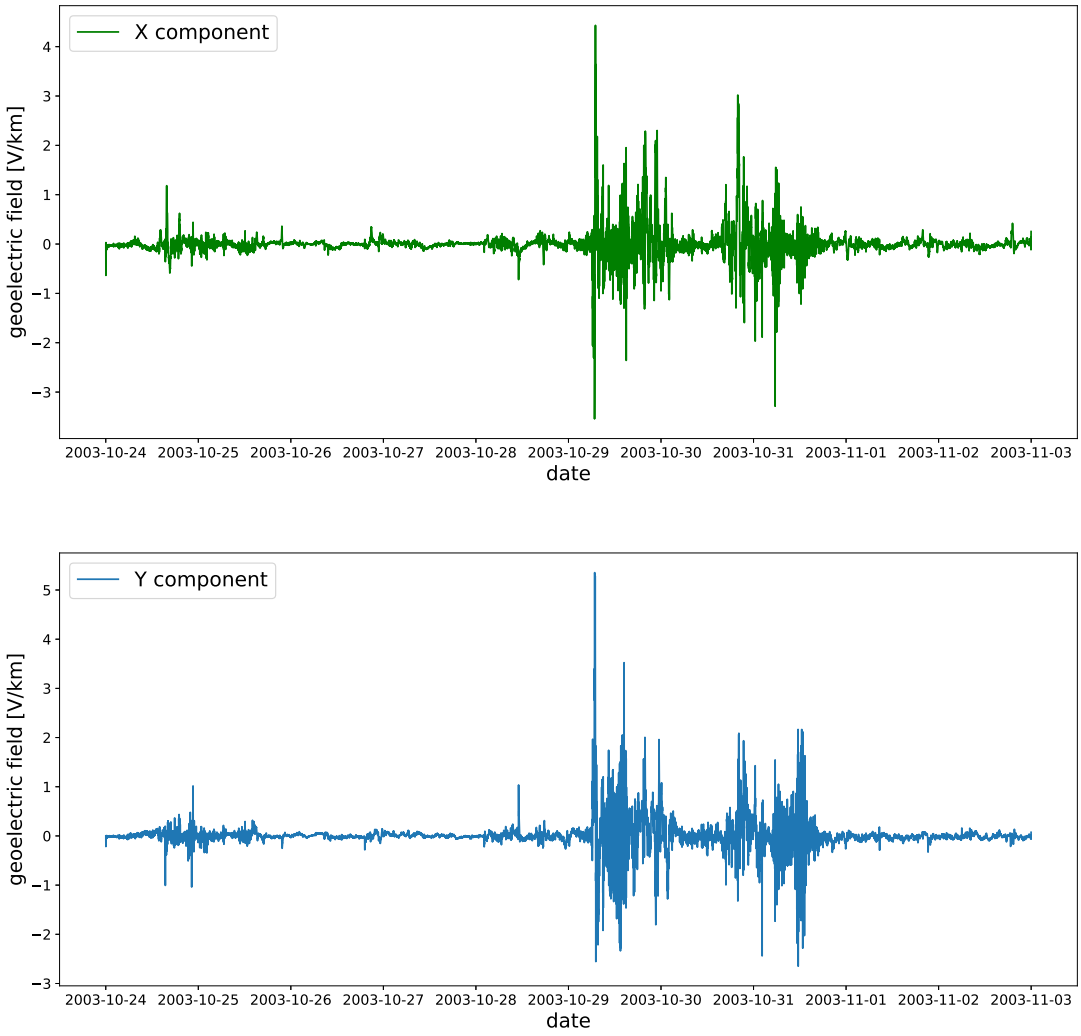

Figure 5.1: North, X, and East, Y, components of the geoelectric field computed by the plane wave model using data from the Budkov Observatory during the Haloween storm in 2003.

increased solar activity that can be measured or observed on the Earth. We found ten dates of auroral display during the years 2005 to 2017 (see Table 5.1) for which we computed the geoelectric field from variations of the geomagnetic field, see demonstrative graphs of the geoelectric field variations on 5 the Haloween storm in 2003 Figure 5.1. A complete set for all remaining dates of aurorae observations in the Czech Republic is then given in Figure A.8–A.17 in the Attachments.

Our program found maximum value of both X and Y components of geoelectric field (E_x and E_y) and computed the corresponding currents from (5.20). Both geoelectric field and induced currents are given in Table 5.2 for dates with aurora observation in the region of the Czech Republic.

Date	Comment
21–22.01.2005	evening 21.1.2005, visible from several places
14–15.12.2006	very weak, second half of the night
05–06.08.2011	visible around midnight
26–27.09.2011	weak, brighter during second half of the night, 23:00–23:30
27–28.02.2014	weak, 23h CET
07–08.09.2015	weak, can be observed by camera, before midnight
20–21.12.2015	weak, several onsets 17:15, 19:10, 21:00 and after 0:35 CET
06–07.03.2016	very weak, shortly after 23h
08–09.05.2016	observable only by camera, around 22:15 CET
27–28.03.2017	weak, can be observed by camera, around 21:50 CET

Table 5.1: Dates for aurora observations in Czech Republic with comments as it is exposed on ukazy.astro.cz website

Date	E_x[V/km]	J_x[A]	E_y[V/km]	J_y[A]
21.01.2005	0.81	38.42	0.55	19.16
14.12.2006	0.52	24.52	0.44	15.1
05.08.2011	0.57	26.87	0.38	13.06
26.09.2011	0.42	19.93	0.49	16.85
27.02.2014	0.25	11.9	0.19	6.41
07.09.2015	0.55	25.92	0.23	7.85
20.12.2015	0.43	20.6	0.37	12.83
06.03.2016	0.35	16.74	0.21	7.3
08.05.2016	0.36	16.94	0.19	6.59
25.03.2017	0.56	26.31	0.17	5.98

Table 5.2: Dates of aurorae in the Czech Republic and the corresponding geoelectric field and currents entering the two selected transmission lines, one in west–east (X) direction and another in north–south direction (Y)

6. Discussion

We performed a statistical analysis of disturbances recorded in the power transmission grid in the Czech Republic similar to the analysis done by Schrijver and Mitchell [2013] for the US power grid. We were looking for a relationship between disturbances reported in the power grid represented by the failure log from Czech distributors with the behaviour of the geomagnetic activity described by the K index. The correlation coefficient between these two series is practically zero as it was expected since there is an unknown time lag between the effects of the increased solar activity and disturbances on the power grid. Moreover, induction of GIC in the conductive structured depends on many factors (solar wind, the structure of Earth's magnetic field, Earth's conductivity, the structure of the power grid) and differ from one power grid to another. Similar result was obtained in Schrijver and Mitchell [2013].

So we needed to apply proper statistical tests to estimate the statistical significance of our working hypothesis saying that the number of recorded disturbances on the power grid is connected to increased geomagnetic activity. In such case, the number of failures recorded during the period of increased geomagnetic active days N_h should be the largest, the number of failures recorded during the period of geomagnetic inactive days N_l should be the smallest and then the number of disturbances for randomly selected intervals should lie between these two numbers because randomly selected interval include geomagnetic active days as well as geomagnetic inactive days.

Results were strongly affected by the selected lengths of the intervals which in practice meant that we took into account only intervals of length between 30 to 70 days. Too short intervals (under the 30 days) increased the noise level because lesser numbers of disturbances fell into the tested intervals and shallower maxima and minima were presented due to smaller smoothing. There was a problem with larger interval lengths too. Requirement of the of non-overlapping neighbouring pairs was in this case quite strong and secular trends of the power grid could appear since maximum–minimum pairs were hundreds of days apart.

We found that in cases of high and very high-voltage transmission lines there were a statistically significant increase in the number of failures with increased geomagnetic activity. Furthermore, for these datasets, there is a relative increase in mean daily failure rate after the local maxima rather than before it. We observe an average increase of the failure rates by $(0.3 - 0.7)\sigma$ after the local maxima. The relative increase I_r results from 7 to 70 percent. Indeed, there is a strong hint of a statistical significance of increase in the failure rates after the maximum of the geomagnetic activity.

On the other hand, no significant differences between failure rates during geomagnetic maximum and geomagnetic minimum were registered on the low-voltage and short-transmission lines. We expected this result because the distances between grounded points are too shorts for inducing sufficient GICs in case of short-transmission line. Low-voltage transmission lines include a mixture of all possible disturbances since they connect high-voltage transmission lines with consumers. Some datasets contain a small number of recorded disturbances so their statistical significance is not credible. We did not compute the relative increase I_r

for these datasets. The statistical significance between the number of recorded disturbances before and after the local maxima of geomagnetic activity is low.

As we know from previous chapters, geomagnetic variations are always accompanied by variations of the geoelectric field which in turn gives rise to GICs in the conductive structures on the Earth. GICs are the only measurable manifestation of the solar activity effects on the Earth except for the observation of polar lights. We can either measure them or model them from the geoelectric field or magnetospheric-ionospheric currents. However, their modelling includes detailed information about technical parameters of the transmission network (admittance matrices, the direction of transmission lines, specific resistivity ...) and we, unfortunately, do not dispose with them.

Since no equipment for measuring of the electric field have been installed in the Czech Republic yet, we were forced to compute it from variations of the magnetic field by our own. We used the plane wave uniform conductive Earth model, where we neglected the curvature of the Earth, assumed that conductivity is $\sigma = 10^{-3}$ Ω^{-1} m and that electric and magnetic field propagate as a plane wave. These assumptions may seem to be too rough but in the case of a small region of the Czech Republic and for the purposes of our study there are sufficient. Besides that, as it was proved by Hejda and Bochníček [2005] and they dealt with the modelling of GIC in pipelines in the Czech Republic the simplest plane wave and uniform conductivity Earth model of the electric field corresponded well to the measurements of pipe-to-soil geovoltages.

Within dates when aurora was observed in the Czech Republic we computed variations of the geoelectric field with an agreement with the previous study of GIC induced in pipelines in the Czech Republic [Hejda and Bochníček, 2005]. We were trying to find whether the Czech power grid is susceptible to increased geomagnetic activity and GICs, so we decided to make a rough guess on currents induced in the conductive systems. These values vary in tens of amperes and the largest value is about 40 A, which is surprisingly large value for the mid-latitude country such as the Czech Republic where expected currents are in orders of amperes. Bailey et al. [2017] showed that the Austrian power grid is susceptible to large GICs in the range of tens of Amperes. Although hundreds of Amperes can destroy the conductive equipment and transformers, tens of amperes have a cumulative effect and adversely damage the facility for longer period of their exposure to the transmission network which may lead to its damage or malfunction in the end. This is a strong indicator of increased solar activity effects in the Czech power transmission network and disturbances recorded on high and very-high voltage transmission network, where the most adverse effect are expected the most.

Statistical analysis done in this study is the first of this kind performed for the mid-latitude location. Many further studies are needed to fully understand our findings. For instance, the GIC modelling in the network together with an assessment of disturbances split to each of the power lines would give a direct evidence about the influence of GICs on the equipment. Analogous statistical analysis as was done for K index can be done for the behaviour of geoelectric field or GIC with failures logs. It can help to find more information about the relationship between recorded disturbances and variations in $\mathbf{E}$ or induced currents. Having a look at the time when GIC are induced we can compute their magnitude and

test its statistical significance with dates of recorded disturbances. That would, however, require a completely different approach. We would need to study the recorded disturbances on a daily basis, investigating separately the days when the geomagnetic field was very disturbed, possibly by evaluating the time derivative of the horizontal components of the field, and compare these days with the days when the geomagnetic field was very quiet. In such a case, however, we could not investigate all the datasets we have in our hands, simply because some of them are too sparse.

Here, for instance, one could go back to Fig. 2.2 a compare the impact of the solar-activity events (e.g. connected with the recordings of the aurorae in mid-latitudes) with the consecutive evolution of failure rates. There are no obvious hints visible by eye, but a careful investigation in a statistical sense may reveal some details. Even a comparison study with other neighbouring countries would bring new hint into the determination of the effects of solar activity in the Czech power grid.

Conclusion

We were dealing with the impact of increased solar activity and consequently of increased geomagnetic activity on the Earth. We attempted to find out if there is a relationship between failures reported on the key components, e.g. transformers on the grid and increased geomagnetic activity.

We searched for a "correlation" between the occurrence of disturbances in the electric power grid in the Czech Republic and the geomagnetic activity described by the K index. The logs of disturbances were split into twelve different datasets according to the data provider (the company), voltage level, and a class of equipment.

We compared the failure rates in the periods around local maxima of geomagnetic activity with the periods around local minima of geomagnetic activity using statistical methods. We found that in most cases the differences are not statistically significant. However for the datasets which record mostly the disturbances in power lines and electrical substations with the high-voltage and very-high-voltage levels we see a statistically significant increase of the number of disturbances in the period of the increased geomagnetic activity when the accumulation windows of a few tens of days are used. The relative increase is roughly between 10 and 70 per cent.

In the dataset recording the disturbances on transformers we see an increase, but we can't reject the null hypothesis that the apparent increase is (probably) due to chance (the case of D8, high-voltage transformers), even though the probability is low (about 8% is a bit larger than the 5% rejection threshold). Curiously enough, these datasets also bear an indication that the increase is larger after the local maxima then before it, which is compatible with an interpretation that the increase indeed is due to the larger geomagnetic activity, where the effects of GICs show up with some delay. Such an interpretation is somewhat surprising for the datasets dealing with power lines (D7, D10, D11, D12), where one does not expect cumulative effects due to the exposure to GICs, but rather an immediate response to the GICs entrance into the electric grid.

Another hint that the disturbances indeed are caused by effects of geomagnetic activity would be if the disturbances occurring in networks of various operators would be somewhat correlated in time. Our code has an option to investigate such an issue. However, as evident from Fig. 2.2, the overlap period of all dataset is short, about three years. Such a length is way too short to obtain any statistically meaningful results. The poor common coverage is, unfortunately, a consequence of years-long delicate negotiations with the data providers.

In the second part of my diploma thesis, we did model geoelectric field from variations of the magnetic field. Using plane wave, the uniform conductive model of the Earth and Maxwell's equations we got integro–differential equation which we solved numerically in Python. Afterwards, we estimated GIC entering the two longest transmission lines

- V413, approximated as a transmission line in the west–east direction only, with a length of 284 km and specific resistance of 0.0289 $\Omega\,\mathrm{km}^{-1}$
- V475, approximated as a transmission line in the north–south direction only, with a length of 138 km and specific resistance of 0.0211 $\Omega\,\mathrm{km}^{-1}$

At first we computed induced geovoltage as a line integral from geoelectric field determined before along the transmission line and subsequently, this value was divided by the specific resistance and so we obtained induced geocurrents. Their values range in tens of Amperes and so may have a cumulative damaging effect on conductive structures. The largest value about 40 Amperes is a strong indicator of effects of increased solar and so geomagnetic activity in power transmission lines.

Together with the results from our statistical analysis of disturbances recorded in Czech power grid with modelling of geoelecric field and/or induced GICs bear susceptibility of Czech power grid to increased solar activity or geomagnetic activity, at least in cases when we expect them to show up. We are speaking about the high and very high-voltage transmission lines. We did not find this kind of significant increase of failure logs for short and low-voltage transmission lines which is still in agreement with our hypothesis. The effects of increased solar activity are not expected to manifest on these type of power lines.

Bibliography

H. M. Antia, A. Bhatnagar, and P. Ulmschneider. *Lectures on solar physics*, volume 619. Springer Science & Business Media, 2003.

R. L. Bailey, T. S. Halbedl, I. Schattauer, A. Römer, G. Achleitner, C. D. Beggan, V. Wesztergom, R. Egli, and R. Leonhardt. Modelling geomagnetically induced currents in midlatitude central europe using a thin-sheet approach. *Annales Geophysicae*, 35:751–761, 2017.

S. J. Bame, J. R. Asbridge, W. C. Feldman, and J. T. Gosling. Evidence for a structure-free state at high solar wind speeds. *Journal of Geophysical Research*, 82(10):1487–1492, 1977.

D. Beamish, T. D. G. Clark, E. Clarke, and A. W. P. Thomson. Geomagnetically induced currents in the uk: geomagnetic variations and surface electric fields. *Journal of atmospheric and solar-terrestrial physics*, 64(16):1779–1792, 2002.

J. W. Belcher and L. Davis Jr. Large-amplitude alfvén waves in the interplanetary medium, 2. *Journal of Geophysical Research*, 76(16):3534–3563, 1971.

R. E. Benestad. Solar activity. *Solar Activity and Earth's Climate*, pages 45–87, 2006.

A. O. Benz. Flare observations. *Living reviews in solar physics*, 14(1):2, 2017.

L. Bolduc. Gic observations and studies in the hydro-Québec power system. *Journal of Atmospheric and Solar-Terrestrial Physics*, 64(16):1793–1802, 2002.

D. H. Boteler, R. J. Pirjola, and H. Nevanlinna. The effects of geomagnetic disturbances on electrical systems at the Earth's surface. *Advances in Space Research*, 22(1):17–27, 1998.

M. Brož and M. Šolc. *Fyzika sluneční soustavy*. Matfyzpress, 2013.

R. C. Carrington. Description of a singular appearance seen in the sun on september 1, 1859. *Monthly Notices of the Royal Astronomical Society*, 20:13–15, 1859.

N. A. Case, A. Grocott, S. E. Milan, T. Nagai, and J. P. Reistad. An analysis of magnetic reconnection events and their associated auroral enhancements. *Journal of Geophysical Research: Space Physics*, 122(3):2922–2935, 2017.

E. W. Cliver and W. F. Dietrich. The 1859 space weather event revisited: limits of extreme activity. *Journal of Space Weather and Space Climate*, 3:31, 2013.

S. W. H. Cowley. A qualitative study of the reconnection between the earth's magnetic field and an interplanetary field of arbitrary orientation. *Radio Science*, 8(11):903–913, 1973.

E. A. Eroshenko, A. V. Belov, D. Boteler, S. P. Gaidash, S. L. Lobkov, R. Pirjola, and L. Trichtchenko. Effects of strong geomagnetic storms on northern railways in russia. *Advances in Space Research*, 46(9):1102–1110, 2010.

S. E. Forbush. On the effects in cosmic-ray intensity observed during the recent magnetic storm. *Physical Review*, 51(12):1108, 1937.

E. Friis-Christensen. Solar variability and climate–a summary. *Space Science Reviews*, 94(1):411–421, 2000.

C. T. Gaunt and G. Coetzee. Transformer failures in regions incorrectly considered to have low gic-risk. In *2007 IEEE Lausanne Power Tech*, pages 807–812. IEEE, 2007.

J. T. Gosling and V. J. Pizzo. Formation and evolution of corotating interaction regions and their three dimensional structure. In *Corotating interaction regions*, pages 21–52. Springer, 1999.

A. Hanslmeier. The sun and space weather. In *Heliophysical Processes*, pages 233–249. Springer, 2010.

B. Heber, T. R. Sanderson, and M. Zhang. Corotating interaction regions. *Advances in Space Research*, 23(3):567–579, 1999.

P. Hejda and J. Bochníček. Geomagnetically induced pipe-to-soil voltages in the czech oil pipelines during october–november 2003. *Annales Geophysicae*, 23: 3089–3093, 2005.

R. Hodgson. On a curious appearance seen in the sun. *Monthly Notices of the Royal Astronomical Society*, 20:15–16, 1859.

J. G. Kappenman. Storm sudden commencement events and the associated geomagnetically induced current risks to ground-based systems at low-latitude and midlatitude locations. *Space weather*, 1(3), 2003.

M. Karlický. *Plasma astrophysics*, volume 162. MatfyzPress, 2014.

H. Koskinen and R. Vainio. Lectures on solar physics: From the core to the heliopause. *Universidade de Helsinki–Finlândia*, 2009.

H. Koskinen, E. Tanskanen, R. Pirjola, A. Pulkkinen, C. Dyer, D. Rodgers, P. Cannon, J. C. Mandeville, D. Boscher, and A. Hilgers. Space weather effects catalogue. *ESA Space Weather Study (ESWS)*, (2.2), 2001.

A. S. Krieger, A. F. Timothy, and E. Roelof. A coronal hole and its identification as the source of a high velocity solar wind stream. *Solar Physics*, 29(2):505–525, 1973.

J. J. Love and A. Swidinsky. Time causal operational estimation of electric fields induced in the earth's lithosphere during magnetic storms. *Geophysical Research Letters*, 41(7):2266–2274, 2014.

J. G. Luhman. Cmes and space weather. *GEOPHYSICAL MONOGRAPH-AMERICAN GEOPHYSICAL UNION*, 99:291–299, 1997.

H. Lundstedt. The sun, space weather and gic effects in sweden. *Advances in Space Research*, 37(6):1182–1191, 2006.

O. E. Malandraki and N. B. Crosby. *Solar Particle Radiation Storms Forecasting and Analysis: The HESPERIA HORIZON 2020 Project and Beyond*, volume 444. Springer, 2018.

O. E. Malandraki, E. T. Sarris, and G. Tsiropoula. Magnetic topology of coronal mass ejection events out of the ecliptic: Ulysses/hi-scale energetic particle observations. In *Annales Geophysicae*, volume 21, pages 1249–1256, 2003.

J. T. Mariska. *The solar transition region*, volume 23. Cambridge University Press, 1992.

R. A. Marshall, M. Dalzell, C. L. Waters, P. Goldthorpe, and E. A. Smith. Geomagnetically induced currents in the new zealand power network. *Space Weather*, 10(8), 2012.

R. Mitalas and K. R. Sills. On the photon diffusion time scale for the sun. *The Astrophysical Journal*, 401:759, 1992.

NERC. Report on march 13, 1989 geomagnetic disturbance, 1990. URL `https://www.nerc.com/files/1989-Quebec-Disturbance.pdf`. Accessed:2019-01-21.

E. N. Parker. Dynamics of the interplanetary gas and magnetic fields. *The Astrophysical Journal*, 128:664, 1958.

L. Perrone and G. De Franceschi. Solar, ionospheric and geomagnetic indices. *Annals of Geophysics*, 41(5-6), 1998.

R. Pirjola. Geomagnetically induced currents during magnetic storms. *IEEE Transactions on Plasma Science*, 28(6):1867–1873, 2000.

R. Pirjola and A. Viljanen. Complex image method for calculating electric and magnetic fields produced by an auroral electrojet of finite length. In *Annales Geophysicae*, volume 16, pages 1434–1444. Springer, 1998.

R. J. Pirjola and D. H. Boteler. Geomagnetically induced currents in european high-voltage power systems. In *2006 Canadian Conference on Electrical and Computer Engineering*, pages 1263–1266. IEEE, 2006.

A. Pulkkinen, A. Viljanen, K. Pajunpää, and R. Pirjola. Recordings and occurrence of geomagnetically induced currents in the finnish natural gas pipeline network. *Journal of Applied Geophysics*, 48(4):219–231, 2001.

I. G. Richardson, E. W. Cliver, and H. V. Cane. Sources of geomagnetic storms for solar minimum and maximum conditions during 1972–2000. *Geophysical Research Letters*, 28(13):2569–2572, 2001.

I. G. Richardson, D. F. Webb, J. Zhang, D. B. Berdichevsky, D. A. Biesecker, J. C. Kasper, R. Kataoka, J. T. Steinberg, B. J. Thompson, C. C. Wu, et al. Major geomagnetic storms (dst $\leq$-100 nt) generated by corotating interaction regions. *Journal of Geophysical Research: Space Physics*, 111(A7), 2006.

C. J. Schrijver and S. D. Mitchell. Disturbances in the us electric grid associated with geomagnetic activity. *Journal of Space Weather and Space Climate*, 3:19, 2013.

C. J. Schrijver and C. Zwaan. *Solar and stellar magnetic activity*, volume 34. Cambridge University Press, 2008.

C. J. Schrijver, . Dobbins, W. Murtagh, and S. M. Petrinec. Assessing the impact of space weather on the electric power grid based on insurance claims for industrial electrical equipment. *Space Weather*, 12(7):487–498, 2014.

K. Shibata and T. Magara. Solar flares: magnetohydrodynamic processes. *Living Reviews in Solar Physics*, 8(1):6, 2011.

S. M. Silverman and E. W. Cliver. Low-latitude auroras: the magnetic storm of 14–15 may 1921. *Journal of Atmospheric and Solar-Terrestrial Physics*, 63(5): 523–535, 2001.

E. A. Spiegel and J. P. Zahn. The solar tachocline. *Astronomy and Astrophysics*, 265:106–114, 1992.

O. C. St Cyr, J. T. Burkepile, A. J. Hundhausen, and A. R. Lecinski. A comparison of ground-based and spacecraft observations of coronal mass ejections from 1980–1989. *Journal of Geophysical Research: Space Physics*, 104(A6): 12493–12506, 1999.

J. M. Torta, L. Serrano, J. R. Regué, A. M. Sanchez, and Elionor Roldán. Geomagnetically induced currents in a power grid of northeastern spain. *Space Weather*, 10(6), 2012.

B. T. Tsurutani and W. D. Gonzalez. The interplanetary causes of magnetic storms: A review. *Magnetic storms*, 98:77–89, 1997.

B. T. Tsurutani, O .P. Verkhoglyadova, A.J. Mannucci, G.S. Lakhina, G. Li, and G. P. Zank. A brief review of "solar flare effects" on the ionosphere. *Radio Science*, 44(1), 2009.

I. G Usoskin, L. Desorgher, P. Velinov, M. Storini, E. O Flückiger, R. Bütikofer, and G. A. Kovaltsov. Ionization of the earth's atmosphere by solar and galactic cosmic rays. *Acta Geophysica*, 57(1):88–101, 2009.

R. F. Wimmer-Schweingruber, P. Bochsler, and G. Gloeckler. The isotopic composition of oxygen in the fast solar wind: Ace/swims. *Geophysical research letters*, 28(14):2763–2766, 2001.

J. J. Zhang, C. Wang, T. R. Sun, C. M. Liu, and K. R. Wang. Gic due to storm sudden commencement in low-latitude high-voltage power network in china: Observation and simulation. *Space Weather*, 13(10):643–655, 2015.

I. P. Zois. Solar activity and transformer failures in the greek national electric grid. *Journal of Space Weather and Space Climate*, 3:32, 2013.

List of Figures

List of Tables

List of Abbreviations

GIC – Geomagnetically induced current
CME – Coronal mass ejection
SEP – Solar energetic particle
IMF – Interplanetary magnetic field
CIR – Corotating interaction region
SIR – Stream interaction region
AU – Astronomical unit
IP – Interplanetary
IMF – Interplanetary magnetic field
EUV – Extreme ultraviaolet
GS – Geomagnetic storm
DST – Disturbance storm-time
FD – Forbush decrease
GCR – Galactic cosmic ray

A. Attachments

A.1 Daily averaged K index

A.2 Results of statistical analysis

A.3 Geoelectric field

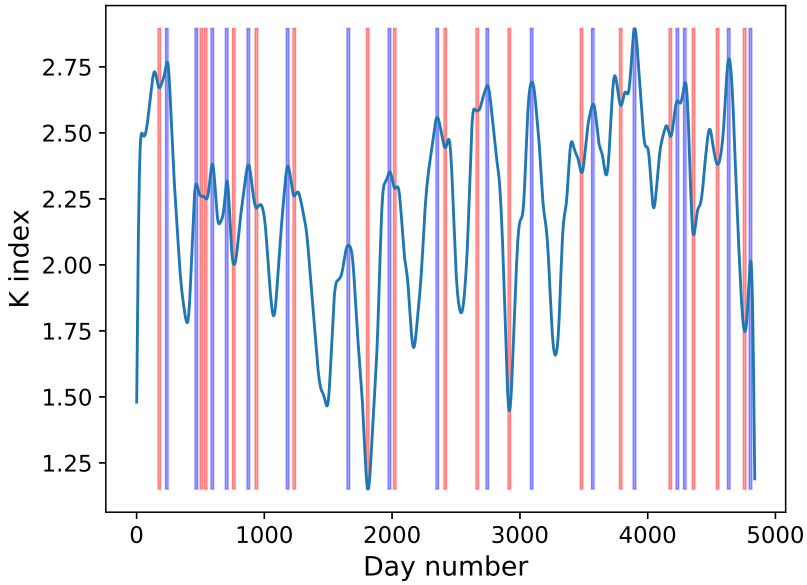

Figure A.1: Daily averaged K index and the pairing of the local maxima (blue) and neighbouring non-overlapping minima (red) detected by our code for $W = 20$.

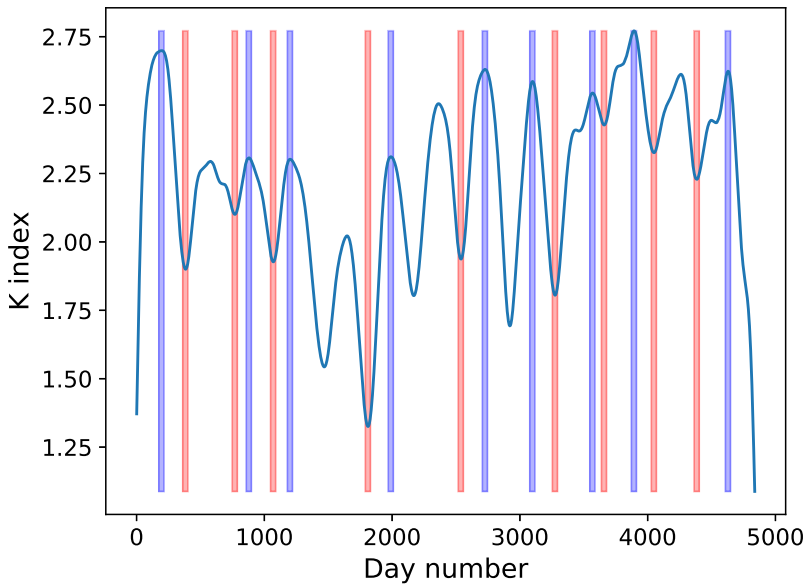

Figure A.2: Daily averaged K index and the pairing of the local maxima (blue) and neighbouring non-overlapping minima (red) detected by our code for $W = 40$.

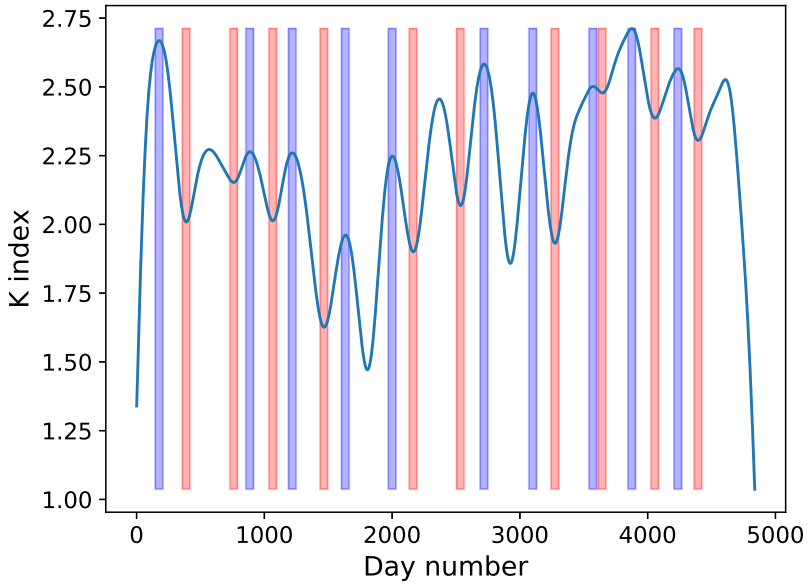

Figure A.3: Daily averaged K index and the pairing of the local maxima (blue) and neighbouring non-overlapping minima (red) detected by our code for $W = 60$.

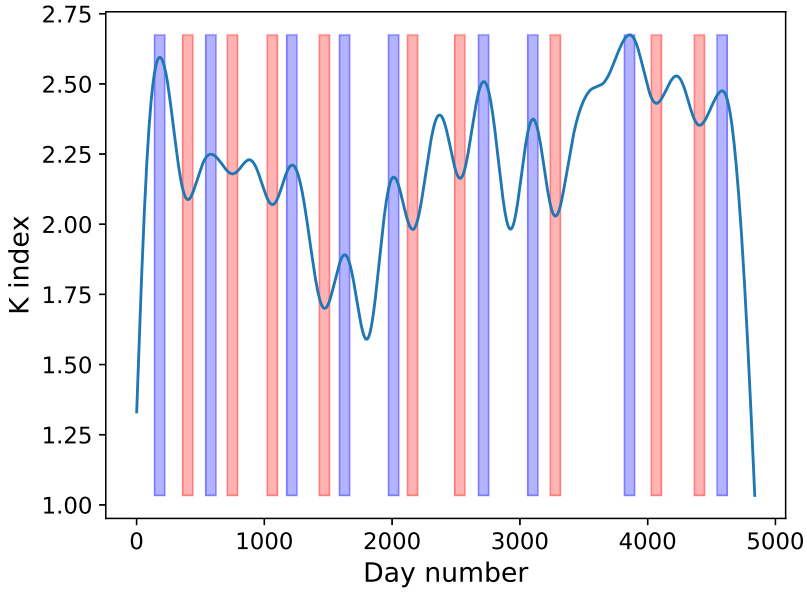

Figure A.4: Daily averaged K index and the pairing of the local maxima (blue) and neighbouring non-overlapping minima (red) detected by our code for $W = 80$.

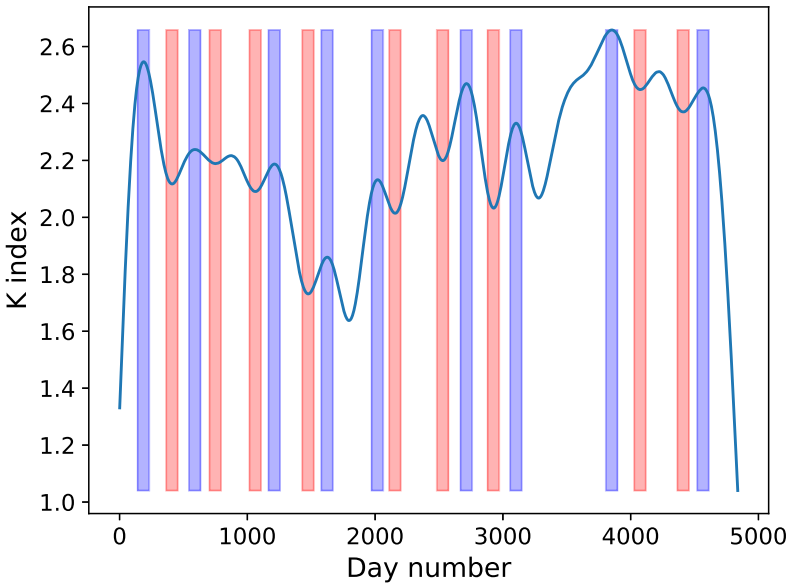

Figure A.5: Daily averaged K index and the pairing of the local maxima (blue) and neighbouring non-overlapping minima (red) detected by our code for $W = 90$.

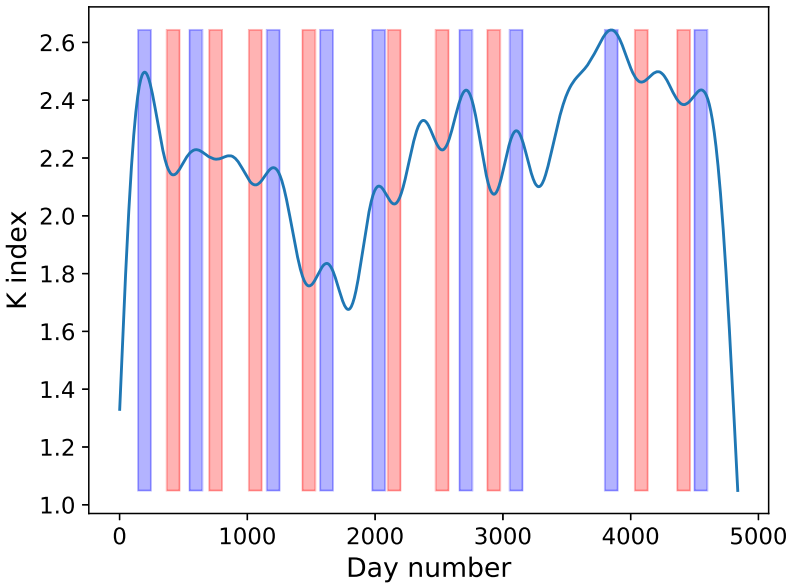

Figure A.6: Daily averaged K index and the pairing of the local maxima (blue) and neighbouring non-overlapping minima (red) detected by our code for $W = 100$.

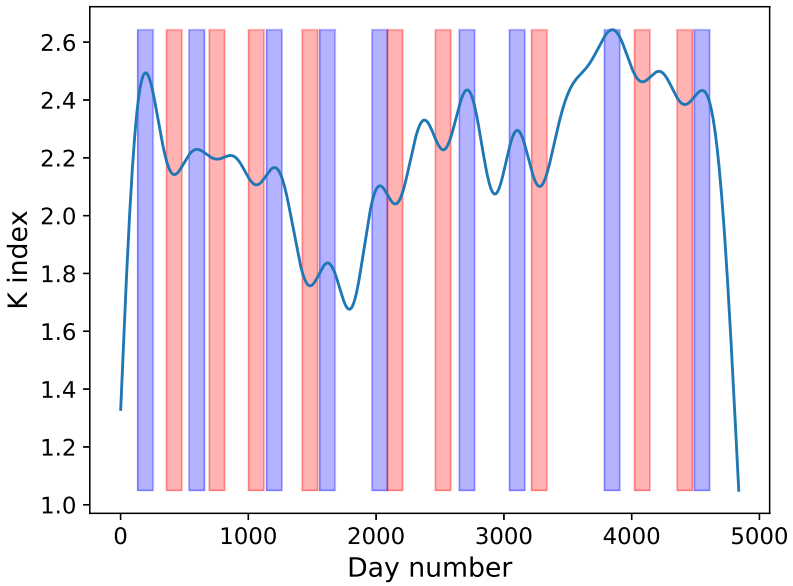

Figure A.7: Daily averaged K index and the pairing of the local maxima (blue) and neighbouring non-overlapping minima (red) detected by our code for $W = 120$.

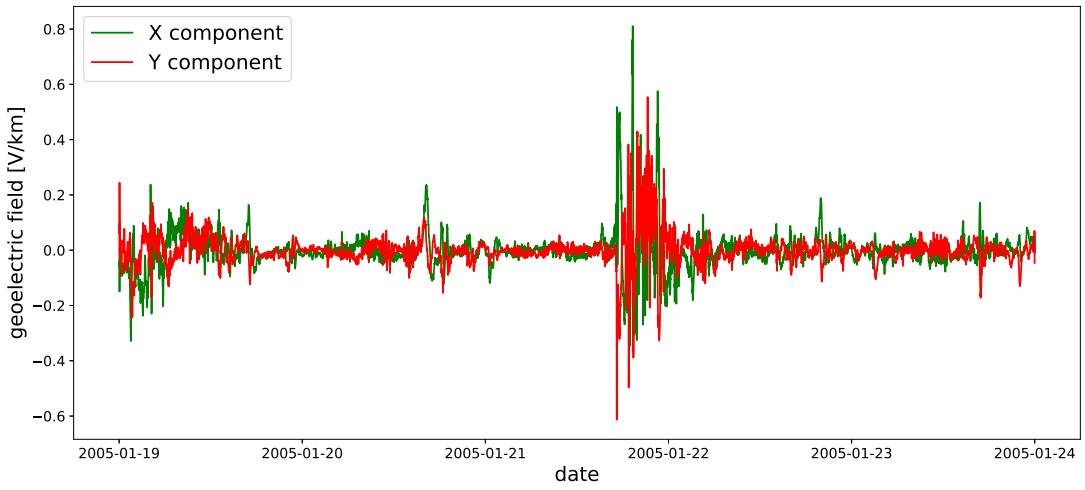

Figure A.8: North, X and East,Y components of the geoelectric field computed by the plane wave model using data from the Budkov Observatory from 19 to 24 January 2005.

Dataset ID	Intervals	N_h	N_r	N_l	$P_\mathrm{h,l}$	$P_\mathrm{r,l}$	$P_\mathrm{h,r}$	a	b	c	d	R	I_r
D1	39	21	20	25	0.65874	1.0	0.55148	21	369	25	365	0.84	–
D2	27	54	62	54	1.0	0.51591	0.51591	54	216	54	216	1.0	–
D3	27	14	14	15	1.0	1.0	1.0	14	256	15	255	0.93333	–
D4	25	16	19	23	0.33678	0.73588	0.64397	16	234	23	227	0.69565	–
D5	25	28	37	37	0.32108	0.32108	1.0	28	222	37	213	0.75676	–
D6	25	13	16	17	0.58466	0.71107	1.0	13	237	17	233	0.76471	–
D7	45	66	7	81	0.24813	$< 10^{-5}$	$< 10^{-5}$	66	384	81	369	0.81481	–
D8	40	436	452	459	0.46213	0.61473	0.84244	245	155	273	127	0.89744	–
D9	40	51	34	49	0.92041	0.08205	0.12385	46	354	40	360	1.15	–
D10	40	6553	6049	6320	0.04087	1e-05	0.01519	400	0	400	0	1.0	< 0.01
D11	40	185	179	197	0.57362	0.79331	0.38067	126	274	141	259	0.89362	–
D12	40	5045	4984	5272	0.02608	0.54909	0.0046	398	2	398	2	1.0	–

Table A.1: Statistical analysis of disturbances in the Czech distribution network for the 10-day window. For datasets D1–D12 we give the number of interval pairs, the total number of reported disturbances in the periods of increased activity, decreased activity, and in the random intervals. Then we give the probabilities P with which the differences in the number of failures between two intervals are due to chance. In the last section we give necessary values for the computation of the relative risk R and also the value of I_r.

Dataset ID	Intervals	N_{h}	N_{r}	N_{l}	$P_{\mathrm{h,l}}$	$P_{\mathrm{r,l}}$	$P_{\mathrm{h,r}}$	a	b	c	d	R	I_{r}
D1	12	18	16	20	0.87141	0.86417	0.61772	18	222	20	220	0.9	–
D2	7	21	35	36	0.06274	0.08143	1.0	21	119	36	104	0.58333	–
D3	7	7	4	7	1.0	0.54883	0.54883	7	133	7	133	1.0	–
D4	7	8	10	14	0.28628	0.81453	0.54126	8	132	14	126	0.57143	–
D5	7	18	16	22	0.63583	0.86417	0.41769	18	122	22	118	0.81818	–
D6	7	9	6	10	1.0	0.60724	0.4545	9	131	10	130	0.9	–
D7	12	46	4	36	0.32029	$< 10^{-5}$	$< 10^{-5}$	46	194	36	204	1.27778	–
D8	11	217	215	250	0.13858	0.96163	0.11477	127	93	139	81	0.91367	–
D9	11	29	23	29	1.0	0.48846	0.48846	25	195	24	196	1.04167	–
D10	11	3861	3786	3807	0.54502	0.39743	0.81847	220	0	220	0	1.0	–
D11	11	141	135	112	0.07814	0.7635	0.16143	94	126	76	144	1.23684	–
D12	11	3125	3209	3030	0.23085	0.297	0.02422	219	1	220	0	0.99545	–

Table A.2: Statistical analysis of disturbances in the Czech distribution network for the 20-day window. For datasets D1–D12 we give the number of interval pairs, the total number of reported disturbances in the periods of increased activity, decreased activity, and in the random intervals. Then we give the probabilities P with which the differences in the number of failures between two intervals are due to chance. In the last section we give necessary values for the computation of the relative risk R and also the value of I_{r}.

Dataset ID	Intervals	N_{h}	N_{r}	N_{l}	$P_{\mathrm{h,l}}$	$P_{\mathrm{r,l}}$	$P_{\mathrm{h,r}}$	a	b	c	d	R	I_{r}
D1	6	24	8	7	0.00333	0.007	1.0	24	216	7	233	3.42857	0.14
D2	4	44	32	33	0.2543	0.20674	1.0	44	116	33	127	1.33333	–
D3	4	7	7	7	1.0	1.0	1.0	7	153	7	153	1.0	–
D4	4	7	14	12	0.35928	0.18925	0.84502	7	153	12	148	0.58333	–
D5	4	22	33	18	0.63583	0.177	0.04887	22	138	18	142	1.22222	–
D6	4	15	10	8	0.21004	0.42436	0.81453	15	145	8	152	1.875	–
D7	8	60	2	25	0.00019	$< 10^{-5}$	1e-05	60	260	25	295	2.4	0.28
D8	6	260	249	247	0.59412	0.65763	0.96419	151	89	130	110	1.16154	–
D9	6	25	35	32	0.42704	0.24506	0.80719	24	216	26	214	0.92308	–
D10	6	4183	3716	3548	$< 10^{-5}$	$< 10^{-5}$	0.05006	240	0	240	0	1.0	0.11
D11	6	123	109	48	$< 10^{-5}$	0.39343	$< 10^{-5}$	92	148	42	198	2.19048	0.6
D12	6	3379	3083	2765	$< 10^{-5}$	0.00024	3e-05	239	1	240	0	0.99583	0.14

Table A.3: Statistical analysis of disturbances in the Czech distribution network for the 40-day window. For datasets D1–D12 we give the number of interval pairs, the total number of reported disturbances in the periods of increased activity, decreased activity, and in the random intervals. Then we give the probabilities P with which the differences in the number of failures between two intervals are due to chance. In the last section we give necessary values for the computation of the relative risk R and also the value of I_{r}.

Dataset ID	Intervals	N_h	N_r	N_l	$P_\mathrm{h,l}$	$P_\mathrm{r,l}$	$P_\mathrm{h,r}$	a	b	c	d	R	I_r
D1	7	43	24	20	0.00515	0.02712	0.65159	43	377	20	400	2.15	0.07
D2	4	64	41	51	0.26305	0.0313	0.34814	64	176	51	189	1.2549	–
D3	4	7	5	12	0.35928	0.77441	0.14346	7	233	12	228	0.58333	–
D4	4	11	22	18	0.26493	0.08014	0.63583	11	229	18	222	0.61111	–
D5	4	32	24	26	0.51184	0.34968	0.88772	32	208	26	214	1.23077	–
D6	4	21	7	10	0.07076	0.01254	0.62906	21	219	10	230	2.1	–
D7	8	75	14	37	0.00042	$< 10^{-5}$	0.00177	75	405	37	443	2.02703	0.19
D8	7	479	434	432	0.12745	0.1453	0.97289	265	155	245	175	1.08163	–
D9	7	38	92	45	0.51041	$< 10^{-5}$	7e-05	36	384	39	381	0.92308	–
D10	7	7516	6550	6242	$< 10^{-5}$	$< 10^{-5}$	0.00664	420	0	420	0	1.0	0.15
D11	7	239	157	96	$< 10^{-5}$	4e-05	0.00015	162	258	76	344	2.13158	0.76
D12	7	6221	5078	4715	$< 10^{-5}$	$< 10^{-5}$	0.00025	419	1	420	0	0.99762	0.25

Table A.4: Statistical analysis of disturbances in the Czech distribution network for the 60-day window. For datasets D1–D12 we give the number of interval pairs, the total number of reported disturbances in the periods of increased activity, decreased activity, and in the random intervals. Then we give the probabilities P with which the differences in the number of failures between two intervals are due to chance. In the last section we give necessary values for the computation of the relative risk R and also the value of I_r.

Dataset ID	Intervals	N_h	N_r	N_l	$P_\mathrm{h,l}$	$P_\mathrm{r,l}$	$P_\mathrm{h,r}$	a	b	c	d	R	I_r
D1	6	31	17	17	0.05946	0.05946	1.0	31	449	17	463	1.82353	–
D2	3	71	45	47	0.03379	0.01988	0.91704	71	169	47	193	1.51064	< 0.01
D3	3	7	10	9	0.80362	0.62906	1.0	7	233	9	231	0.77778	–
D4	3	14	24	17	0.7201	0.14331	0.34889	14	226	17	223	0.82353	–
D5	3	36	32	26	0.25285	0.7163	0.51184	36	204	26	214	1.38462	–
D6	3	22	11	11	0.08014	0.08014	1.0	22	218	11	229	2.0	–
D7	7	119	8	33	$< 10^{-5}$	$< 10^{-5}$	0.00011	119	441	33	527	3.60606	1.05
D8	6	544	446	465	0.01403	0.00203	0.55095	300	180	281	199	1.06762	< 0.01
D9	6	48	87	52	0.76435	0.001	0.00377	46	434	46	434	1.0	–
D10	6	8504	7539	6985	$< 10^{-5}$	$< 10^{-5}$	$< 10^{-5}$	480	0	480	0	1.0	0.17
D11	6	305	220	117	$< 10^{-5}$	0.00024	$< 10^{-5}$	205	275	90	390	2.27778	0.91
D12	6	7079	5814	5311	$< 10^{-5}$	$< 10^{-5}$	$< 10^{-5}$	478	2	479	1	0.99791	0.27

Table A.5: Statistical analysis of disturbances in the Czech distribution network for the 80-day window. For datasets D1–D12 we give the number of interval pairs, the total number of reported disturbances in the periods of increased activity, decreased activity, and in the random intervals. Then we give the probabilities P with which the differences in the number of failures between two intervals are due to chance. In the last section we give necessary values for the computation of the relative risk R and also the value of I_r.

Dataset ID	Intervals	N_h	N_r	N_l	$P_\mathrm{h,l}$	$P_\mathrm{r,l}$	$P_\mathrm{h,r}$	a	b	c	d	R	I_r
D1	6	32	43	25	0.42704	0.24805	0.03846	32	508	25	515	1.28	–
D2	3	80	53	51	0.01412	0.0238	0.92195	80	190	51	219	1.56863	< 0.01
D3	3	9	14	11	0.8238	0.40487	0.69004	9	261	11	259	0.81818	–
D4	3	16	15	20	0.61772	1.0	0.49956	16	254	20	250	0.8	–
D5	3	39	31	23	0.0559	0.40296	0.34089	39	231	23	247	1.69565	–
D6	3	23	18	4	0.00031	0.53271	0.00434	23	247	4	266	5.75	0.44
D7	7	133	8	34	$< 10^{-5}$	$< 10^{-5}$	7e-05	133	497	34	596	3.91176	1.25
D8	6	599	477	551	0.16573	0.00022	0.02275	336	204	320	220	1.05	–
D9	6	57	68	52	0.70181	0.37116	0.17065	54	486	46	494	1.17391	–
D10	6	9440	8771	7917	$< 10^{-5}$	$< 10^{-5}$	$< 10^{-5}$	540	0	540	0	1.0	0.14
D11	6	332	200	141	$< 10^{-5}$	$< 10^{-5}$	0.00165	225	315	108	432	2.08333	0.77
D12	6	7945	6360	6105	$< 10^{-5}$	$< 10^{-5}$	0.0229	538	2	539	1	0.99814	0.24

Table A.6: Statistical analysis of disturbances in the Czech distribution network for the 90-day window. For datasets D1–D12 we give the number of interval pairs, the total number of reported disturbances in the periods of increased activity, decreased activity, and in the random intervals. Then we give the probabilities P with which the differences in the number of failures between two intervals are due to chance. In the last section we give necessary values for the computation of the relative risk R and also the value of I_r.

Dataset ID	Intervals	N_{h}	N_{r}	N_{l}	$P_{\mathrm{h,l}}$	$P_{\mathrm{r,l}}$	$P_{\mathrm{h,r}}$	a	b	c	d	R	I_{r}
D1	7	31	28	30	1.0	0.79484	0.89568	31	669	30	670	1.03333	–
D2	3	83	76	58	0.04288	0.63433	0.14166	83	217	58	242	1.43103	< 0.01
D3	3	9	20	11	0.8238	0.06143	0.14961	9	291	11	289	0.81818	–
D4	3	17	21	22	0.5224	0.6271	1.0	17	283	22	278	0.77273	–
D5	3	42	37	25	0.0498	0.65296	0.16188	42	258	25	275	1.68	< 0.01
D6	3	25	15	4	0.0001	0.15386	0.01921	25	275	4	296	6.25	0.56
D7	7	139	15	39	$< 10^{-5}$	$< 10^{-5}$	0.0015	139	561	39	661	3.5641	1.11
D8	6	665	624	607	0.10996	0.26522	0.64839	379	221	353	247	1.07365	–
D9	6	60	74	53	0.57266	0.26135	0.07553	57	543	47	553	1.21277	–
D10	6	10266	8880	8738	$< 10^{-5}$	$< 10^{-5}$	0.28811	600	0	600	0	1.0	0.13
D11	6	361	346	166	$< 10^{-5}$	0.59856	$< 10^{-5}$	244	356	129	471	1.89147	0.66
D12	6	8584	7437	6831	$< 10^{-5}$	$< 10^{-5}$	$< 10^{-5}$	598	2	599	1	0.99833	0.2

Table A.7: Statistical analysis of disturbances in the Czech distribution network for the 100-day window. For datasets D1–D12 we give the number of interval pairs, the total number of reported disturbances in the periods of increased activity, decreased activity, and in the random intervals. Then we give the probabilities P with which the differences in the number of failures between two intervals are due to chance. In the last section we give necessary values for the computation of the relative risk R and also the value of I_{r}.

Dataset ID	Intervals	N_{h}	N_{r}	N_{l}	$P_{\mathrm{h,l}}$	$P_{\mathrm{r,l}}$	$P_{\mathrm{h,r}}$	a	b	c	d	R	I_{r}
D1	6	35	36	29	0.53231	1.0	0.45702	35	685	29	691	1.2069	–
D2	3	95	50	61	0.00803	0.00023	0.34258	95	265	61	299	1.55738	0.02
D3	3	11	15	11	1.0	0.5572	0.5572	11	349	11	349	1.0	–
D4	3	24	29	27	0.77977	0.58313	0.89385	24	336	27	333	0.88889	–
D5	3	56	68	40	0.12535	0.32325	0.00906	56	304	40	320	1.4	–
D6	3	33	19	17	0.03284	0.07039	0.86794	33	327	17	343	1.94118	< 0.01
D7	7	152	11	51	$< 10^{-5}$	$< 10^{-5}$	$< 10^{-5}$	152	688	51	789	2.98039	0.88
D8	6	778	658	734	0.26879	0.00168	0.04437	447	273	427	293	1.04684	–
D9	6	70	80	66	0.7971	0.46255	0.28194	66	654	60	660	1.1	–
D10	6	12005	11045	10376	$< 10^{-5}$	$< 10^{-5}$	1e-05	720	0	720	0	1.0	0.12
D11	6	403	214	194	$< 10^{-5}$	$< 10^{-5}$	0.3469	279	441	150	570	1.86	0.62
D12	6	10082	10104	8154	$< 10^{-5}$	0.8825	$< 10^{-5}$	718	2	719	1	0.99861	0.19

Table A.8: Statistical analysis of disturbances in the Czech distribution network for the 120-day window. For datasets D1–D12 we give the number of interval pairs, the total number of reported disturbances in the periods of increased activity, decreased activity, and in the random intervals. Then we give the probabilities P with which the differences in the number of failures between two intervals are due to chance. In the last section we give necessary values for the computation of the relative risk R and also the value of I_{r}.

Dataset ID	$\mu_{-\max}$	$\mu_{\max+}$	$\sigma_{-\max}$	$\sigma_{\max+}$	$\mu_{-\min}$	$\mu_{\min+}$	$\sigma_{-\min}$	$\sigma_{\min+}$	$\frac{I_{\max}}{\sigma_{-\max}}$	$\frac{I_{\min}}{\sigma_{-\min}}$	P_{-+}
D1	1.9	2.1	1.7	1.14	3.0	2.3	0.89	1.0	0.118	-0.783	0.42395
D2	6.2	5.4	2.04	1.8	5.7	5.6	1.19	1.91	-0.392	-0.084	0.89385
D3	1.3	1.4	1.1	0.8	1.7	0.7	1.1	0.64	0.091	-0.909	1.0
D4	2.1	1.6	1.04	1.36	2.0	2.0	1.18	1.34	-0.479	0.0	0.62906
D5	3.7	2.8	1.35	1.94	3.5	3.9	1.86	1.51	-0.669	0.215	1.0
D6	2.0	1.3	1.18	1.1	1.8	1.7	1.47	1.0	-0.592	-0.068	1.0
D7	6.7	6.6	2.24	2.2	7.3	8.6	1.27	2.37	-0.045	1.025	0.38173
D8	40.7	43.6	6.5	7.68	44.2	48.0	5.69	7.03	0.446	0.668	0.11141
D9	2.6	5.1	1.74	1.87	4.3	5.2	1.68	2.56	1.434	0.537	0.86794
D10	622.3	655.3	36.87	56.92	611.5	642.6	35.15	51.24	0.895	0.885	0.00028
D11	17.0	18.5	4.1	4.8	19.2	20.9	2.93	3.75	0.366	0.581	0.53354
D12	545.0	504.5	49.28	34.47	504.2	560.2	42.68	44.24	-0.822	1.312	0.21397

Table A.9: Comparison of the failure rates around the local minima and maxima. In the first section we give mean values (μ) and standard deviations (σ) for the intervals of length $W = 10$ days before local maxima (subscript $-\max$) and after the maxima (subscript $\max+$). In the second section analogous parameters are evaluated for local minima. In the third section we give the relative increase of the means in the units of the standard deviation evaluated before the extreme. In the last section we give the probability that the differences in the interval before the maximum and after the maximum are due to chance.

Dataset ID	$\mu_{-\max}$	$\mu_{\max+}$	$\sigma_{-\max}$	$\sigma_{\max+}$	$\mu_{-\min}$	$\mu_{\min+}$	$\sigma_{-\min}$	$\sigma_{\min+}$	$\frac{I_{\max}}{\sigma_{-\max}}$	$\frac{I_{\min}}{\sigma_{-\min}}$	P_{-+}
D1	0.65	0.9	0.79	0.99	0.8	0.75	0.93	0.99	0.316	-0.054	1.0
D2	1.95	1.05	0.92	0.8	1.6	1.85	1.02	1.15	-0.978	0.245	0.37709
D3	0.3	0.35	0.56	0.48	0.2	0.45	0.4	0.67	0.09	0.625	0.375
D4	0.6	0.4	1.07	0.58	0.45	0.9	0.59	0.83	-0.187	0.763	0.72656
D5	1.4	0.9	1.2	0.99	0.85	1.2	0.65	0.98	-0.417	0.535	0.66362
D6	0.8	0.45	0.68	0.59	0.45	0.3	0.59	0.56	-0.516	-0.254	1.0
D7	3.2	2.3	1.72	1.0	1.55	2.0	0.86	1.22	-0.523	0.52	0.59664
D8	12.5	10.85	4.2	3.35	12.6	11.15	4.08	4.33	-0.393	-0.355	0.79755
D9	1.95	1.45	1.43	1.4	1.75	1.3	1.3	1.31	-0.349	-0.346	0.41769
D10	203.6	193.05	32.86	27.47	173.0	188.85	26.36	25.16	-0.321	0.601	0.34944
D11	7.35	7.05	3.66	2.77	4.85	7.45	2.2	4.02	-0.082	1.183	1.0
D12	168.0	156.25	24.89	29.22	141.55	153.0	28.18	38.17	-0.472	0.406	0.44775

Table A.10: Comparison of the failure rates around the local minima and maxima. In the first section we give mean values (μ) and standard deviations (σ) for the intervals of length $W = 20$ days before local maxima (subscript $-\max$) and after the maxima (subscript $\max+$). In the second section analogous parameters are evaluated for local minima. In the third section we give the relative increase of the means in the units of the standard deviation evaluated before the extreme. In the last section we give the probability that the differences in the interval before the maximum and after the maximum are due to chance.

Dataset ID	$\mu_{-\max}$	$\mu_{\max+}$	$\sigma_{-\max}$	$\sigma_{\max+}$	$\mu_{-\min}$	$\mu_{\min+}$	$\sigma_{-\min}$	$\sigma_{\min+}$	$\frac{I_{\max}}{\sigma_{-\max}}$	$\frac{I_{\min}}{\sigma_{-\min}}$	P_{-+}
D1	0.4	0.6	0.54	0.7	0.33	0.23	0.57	0.42	0.371	-0.177	0.62906
D2	0.97	1.1	0.76	0.73	0.75	0.9	0.83	0.89	0.165	0.181	0.76599
D3	0.13	0.17	0.33	0.38	0.17	0.13	0.49	0.33	0.151	-0.101	1.0
D4	0.5	0.17	0.74	0.38	0.25	0.33	0.49	0.52	-0.438	0.154	0.28906
D5	0.82	0.55	0.86	0.63	0.5	0.38	0.59	0.53	-0.319	-0.211	0.5572
D6	0.33	0.38	0.52	0.53	0.3	0.07	0.51	0.26	0.096	-0.441	1.0
D7	1.7	1.5	0.9	0.92	0.6	0.6	0.58	0.62	-0.222	0.0	0.70798
D8	6.13	6.5	2.44	2.43	5.55	5.72	3.0	3.66	0.154	0.058	0.70719
D9	0.68	0.63	0.85	0.83	0.68	0.68	0.72	0.85	-0.059	0.0	0.16864
D10	104.95	104.58	17.93	18.43	81.13	86.0	17.84	23.75	-0.021	0.273	0.12801
D11	3.52	3.08	2.48	1.63	1.2	1.52	1.1	1.24	-0.181	0.295	0.18811
D12	82.65	84.47	15.41	21.24	67.05	64.78	20.64	25.11	0.118	-0.11	0.51651

Table A.11: Comparison of the failure rates around the local minima and maxima. In the first section we give mean values (μ) and standard deviations (σ) for the intervals of length $W = 40$ days before local maxima (subscript $-\max$) and after the maxima (subscript $\max+$). In the second section analogous parameters are evaluated for local minima. In the third section we give the relative increase of the means in the units of the standard deviation evaluated before the extreme. In the last section we give the probability that the differences in the interval before the maximum and after the maximum are due to chance.

Dataset ID	$\mu_{-\max}$	$\mu_{\max+}$	$\sigma_{-\max}$	$\sigma_{\max+}$	$\mu_{-\min}$	$\mu_{\min+}$	$\sigma_{-\min}$	$\sigma_{\min+}$	$\frac{I_{\max}}{\sigma_{-\max}}$	$\frac{I_{\min}}{\sigma_{-\min}}$	P_{-+}
D1	0.37	0.72	0.66	0.9	0.5	0.32	0.56	0.62	0.532	-0.326	0.26493
D2	1.05	1.07	0.96	0.79	0.72	0.73	0.78	0.93	0.017	0.021	0.26781
D3	0.1	0.12	0.3	0.32	0.1	0.13	0.35	0.34	0.056	0.095	1.0
D4	0.57	0.18	0.64	0.39	0.25	0.35	0.43	0.6	-0.597	0.231	0.07835
D5	0.85	0.53	0.7	0.72	0.47	0.4	0.56	0.66	-0.45	-0.119	0.8804
D6	0.32	0.35	0.56	0.6	0.27	0.08	0.44	0.33	0.059	-0.415	0.21004
D7	1.12	1.25	0.78	1.01	0.62	0.5	0.73	0.62	0.172	-0.159	0.28878
D8	6.35	7.98	2.54	3.31	6.83	6.73	2.94	3.1	0.644	-0.034	0.00013
D9	0.78	0.63	1.0	0.73	0.7	0.6	0.8	0.82	-0.15	-0.125	0.00643
D10	116.05	125.27	18.0	22.27	98.13	103.1	17.26	17.76	0.512	0.288	0.01362
D11	4.23	3.98	2.58	2.61	1.42	1.93	1.27	1.55	-0.097	0.407	0.43185
D12	90.0	103.68	16.31	23.09	79.37	76.72	18.82	16.13	0.839	-0.141	0.0

Table A.12: Comparison of the failure rates around the local minima and maxima. In the first section we give mean values (μ) and standard deviations (σ) for the intervals of length $W = 60$ days before local maxima (subscript $-\max$) and after the maxima (subscript $\max+$). In the second section analogous parameters are evaluated for local minima. In the third section we give the relative increase of the means in the units of the standard deviation evaluated before the extreme. In the last section we give the probability that the differences in the interval before the maximum and after the maximum are due to chance.

Dataset ID	$\mu_{-\max}$	$\mu_{\max+}$	$\sigma_{-\max}$	$\sigma_{\max+}$	$\mu_{-\min}$	$\mu_{\min+}$	$\sigma_{-\min}$	$\sigma_{\min+}$	$\frac{I_{\max}}{\sigma_{-\max}}$	$\frac{I_{\min}}{\sigma_{-\min}}$	P_{-+}
D1	0.4	0.39	0.58	0.66	0.3	0.26	0.6	0.49	-0.021	-0.062	0.20049
D2	0.79	0.89	0.72	0.85	0.55	0.49	0.59	0.61	0.139	-0.106	0.30187
D3	0.1	0.09	0.3	0.28	0.11	0.07	0.32	0.26	-0.042	-0.119	1.0
D4	0.39	0.17	0.6	0.47	0.16	0.29	0.4	0.48	-0.353	0.311	0.29621
D5	0.56	0.45	0.65	0.72	0.38	0.33	0.56	0.52	-0.173	-0.09	0.68888
D6	0.2	0.28	0.4	0.55	0.25	0.05	0.46	0.22	0.188	-0.434	0.0169
D7	1.18	1.49	0.85	0.91	0.45	0.38	0.57	0.56	0.368	-0.132	0.14213
D8	5.42	6.8	2.5	3.11	6.34	5.76	3.24	2.53	0.55	-0.177	0.0
D9	0.64	0.6	0.91	0.66	0.6	0.46	0.77	0.69	-0.041	-0.179	0.01266
D10	95.49	106.3	18.37	21.51	83.99	89.55	16.47	17.32	0.589	0.338	0.0
D11	3.52	3.81	2.66	2.3	1.3	1.99	1.21	1.68	0.108	0.569	0.39428
D12	73.31	88.49	18.36	19.86	69.76	67.0	17.22	19.08	0.827	-0.16	0.0

Table A.13: Comparison of the failure rates around the local minima and maxima. In the first section we give mean values (μ) and standard deviations (σ) for the intervals of length $W = 80$ days before local maxima (subscript $-\max$) and after the maxima (subscript $\max+$). In the second section analogous parameters are evaluated for local minima. In the third section we give the relative increase of the means in the units of the standard deviation evaluated before the extreme. In the last section we give the probability that the differences in the interval before the maximum and after the maximum are due to chance.

Dataset ID	$\mu_{-\max}$	$\mu_{\max+}$	$\sigma_{-\max}$	$\sigma_{\max+}$	$\mu_{-\min}$	$\mu_{\min+}$	$\sigma_{-\min}$	$\sigma_{\min+}$	$\frac{I_{\max}}{\sigma_{-\max}}$	$\frac{I_{\min}}{\sigma_{-\min}}$	P_{-+}
D1	0.41	0.36	0.65	0.64	0.33	0.27	0.52	0.44	-0.086	-0.129	0.59661
D2	0.77	0.89	0.8	0.81	0.59	0.53	0.66	0.7	0.152	-0.084	0.59004
D3	0.09	0.1	0.32	0.3	0.11	0.1	0.31	0.3	0.035	-0.035	1.0
D4	0.34	0.18	0.54	0.44	0.17	0.23	0.4	0.5	-0.308	0.166	0.39153
D5	0.5	0.43	0.64	0.65	0.31	0.28	0.57	0.54	-0.105	-0.058	0.69888
D6	0.18	0.26	0.41	0.46	0.14	0.04	0.38	0.21	0.19	-0.262	0.07552
D7	1.06	1.48	0.85	0.98	0.33	0.39	0.56	0.55	0.498	0.1	0.02068
D8	5.61	6.66	2.6	2.91	6.27	5.68	2.62	2.8	0.402	-0.224	1e-05
D9	0.57	0.63	0.78	0.67	0.52	0.53	0.76	0.75	0.086	0.015	0.04794
D10	92.96	104.89	18.97	23.18	83.2	92.31	13.0	17.46	0.629	0.701	0.0
D11	3.46	3.69	2.65	1.94	1.6	1.99	1.35	1.59	0.088	0.288	0.30843
D12	71.61	88.28	18.75	20.17	67.11	68.81	14.42	22.83	0.889	0.118	0.0

Table A.14: Comparison of the failure rates around the local minima and maxima. In the first section we give mean values (μ) and standard deviations (σ) for the intervals of length $W = 90$ days before local maxima (subscript $-\max$) and after the maxima (subscript $\max+$). In the second section analogous parameters are evaluated for local minima. In the third section we give the relative increase of the means in the units of the standard deviation evaluated before the extreme. In the last section we give the probability that the differences in the interval before the maximum and after the maximum are due to chance.

Dataset ID	$\mu_{-\max}$	$\mu_{\max+}$	$\sigma_{-\max}$	$\sigma_{\max+}$	$\mu_{-\min}$	$\mu_{\min+}$	$\sigma_{-\min}$	$\sigma_{\min+}$	$\frac{I_{\max}}{\sigma_{-\max}}$	$\frac{I_{\min}}{\sigma_{-\min}}$	P_{-+}
D1	0.42	0.31	0.74	0.5	0.35	0.34	0.65	0.49	-0.149	-0.015	0.51138
D2	0.74	0.83	0.7	0.8	0.59	0.58	0.69	0.67	0.128	-0.014	0.91704
D3	0.09	0.09	0.32	0.29	0.11	0.09	0.31	0.29	0.0	-0.064	1.0
D4	0.33	0.17	0.55	0.45	0.21	0.25	0.45	0.48	-0.292	0.088	0.24298
D5	0.47	0.42	0.67	0.64	0.36	0.29	0.54	0.5	-0.075	-0.13	0.80131
D6	0.16	0.25	0.37	0.5	0.15	0.05	0.36	0.22	0.245	-0.28	0.05224
D7	0.95	1.39	0.84	0.96	0.37	0.5	0.59	0.64	0.523	0.219	0.20473
D8	5.56	6.65	2.8	2.9	6.29	5.64	2.86	2.88	0.389	-0.227	0.00088
D9	0.53	0.6	0.9	0.77	0.54	0.61	0.77	0.92	0.078	0.091	0.09246
D10	93.1	102.66	20.21	22.96	85.82	91.26	17.13	16.86	0.473	0.318	0.0
D11	3.3	3.61	2.65	2.1	1.79	2.16	1.93	1.73	0.117	0.192	0.05326
D12	71.28	85.84	18.78	21.62	68.93	70.21	16.6	20.75	0.775	0.077	0.0

Table A.15: Comparison of the failure rates around the local minima and maxima. In the first section we give mean values (μ) and standard deviations (σ) for the intervals of length $W = 100$ days before local maxima (subscript $-\max$) and after the maxima (subscript $\max+$). In the second section analogous parameters are evaluated for local minima. In the third section we give the relative increase of the means in the units of the standard deviation evaluated before the extreme. In the last section we give the probability that the differences in the interval before the maximum and after the maximum are due to chance.

Dataset ID	$\mu_{-\max}$	$\mu_{\max+}$	$\sigma_{-\max}$	$\sigma_{\max+}$	$\mu_{-\min}$	$\mu_{\min+}$	$\sigma_{-\min}$	$\sigma_{\min+}$	$\frac{I_{\max}}{\sigma_{-\max}}$	$\frac{I_{\min}}{\sigma_{-\min}}$	P_{-+}
D1	0.38	0.29	0.63	0.52	0.32	0.34	0.56	0.47	-0.144	0.044	0.56006
D2	0.69	0.79	0.78	0.77	0.57	0.53	0.65	0.66	0.128	-0.076	0.70181
D3	0.12	0.09	0.35	0.29	0.12	0.07	0.32	0.25	-0.072	-0.156	1.0
D4	0.33	0.2	0.55	0.44	0.17	0.28	0.4	0.5	-0.241	0.27	0.05958
D5	0.47	0.47	0.63	0.67	0.38	0.33	0.53	0.54	0.0	-0.078	0.81259
D6	0.15	0.28	0.38	0.48	0.22	0.05	0.43	0.22	0.329	-0.386	0.14961
D7	0.85	1.27	0.83	1.01	0.62	0.7	0.81	0.75	0.5	0.103	0.10075
D8	5.49	6.48	2.8	3.06	6.28	5.92	2.83	2.64	0.354	-0.127	0.00091
D9	0.46	0.58	0.71	0.77	0.59	0.59	0.77	0.83	0.177	0.0	0.48868
D10	92.84	100.04	18.71	22.27	88.21	90.54	17.63	16.77	0.385	0.132	0.0
D11	2.87	3.36	2.41	2.18	2.2	2.34	2.12	1.9	0.204	0.067	0.42499
D12	71.38	84.02	22.03	20.27	73.27	70.37	17.46	19.0	0.574	-0.166	0.0

Table A.16: Comparison of the failure rates around the local minima and maxima. In the first section we give mean values (μ) and standard deviations (σ) for the intervals of length $W = 120$ days before local maxima (subscript $-\max$) and after the maxima (subscript $\max+$). In the second section analogous parameters are evaluated for local minima. In the third section we give the relative increase of the means in the units of the standard deviation evaluated before the extreme. In the last section we give the probability that the differences in the interval before the maximum and after the maximum are due to chance.

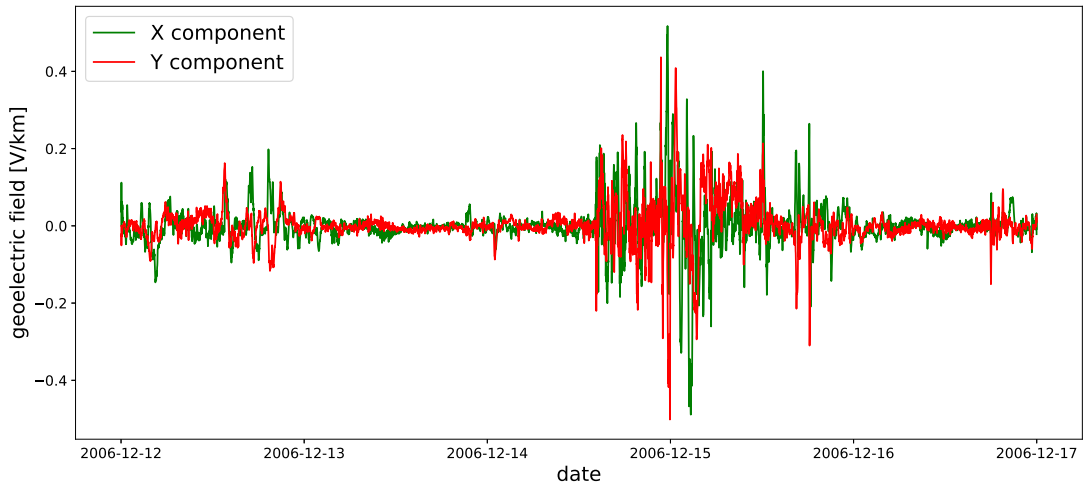

Figure A.9: North, X and East,Y components of the geoelectric field computed by the plane wave model using data from the Budkov Observatory from 12 to 17 December 2006.

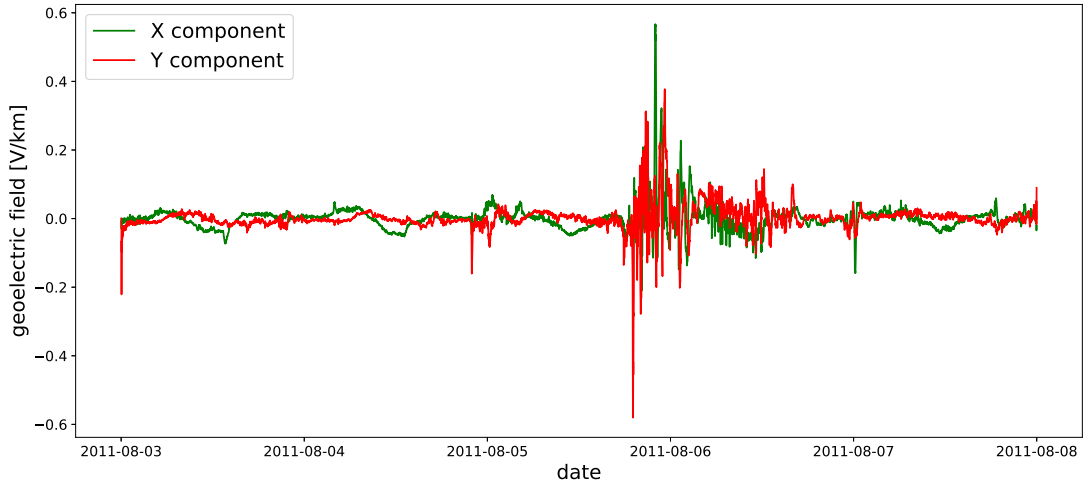

Figure A.10: North, X and East,Y components of the geoelectric field computed by the plane wave model using data from the Budkov Observatory from 3 to 8 August 2011.

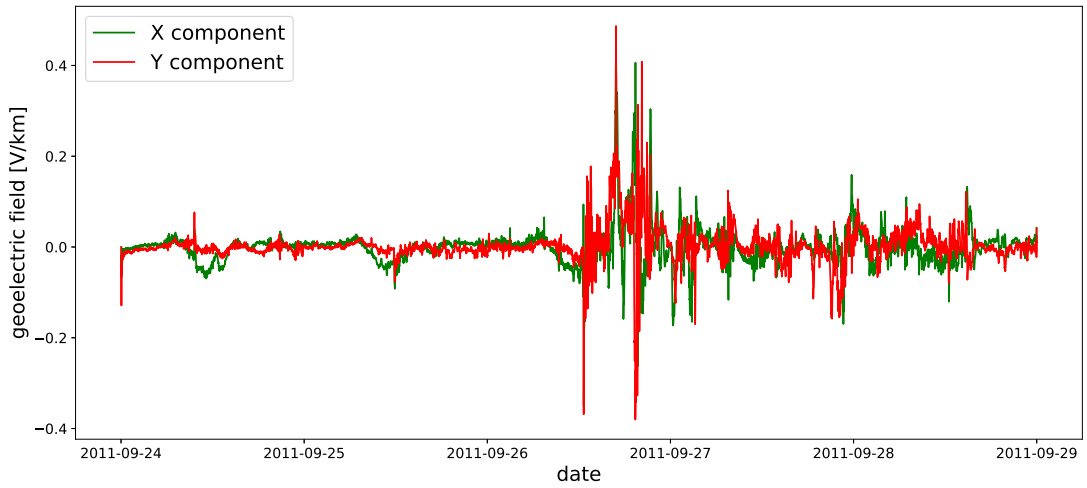

Figure A.11: North, X and East,Y components of the geoelectric field computed by the plane wave model using data from the Budkov Observatory from 24 to 29 November 2011.

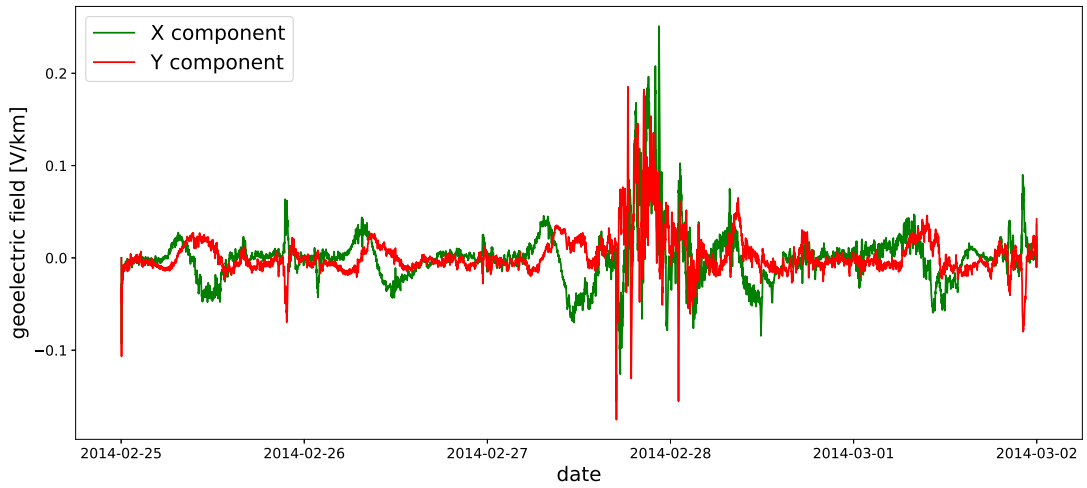

Figure A.12: North, X and East,Y components of the geoelectric field computed by the plane wave model using data from the Budkov Observatory from 25 Febrary to 2 March 2014.

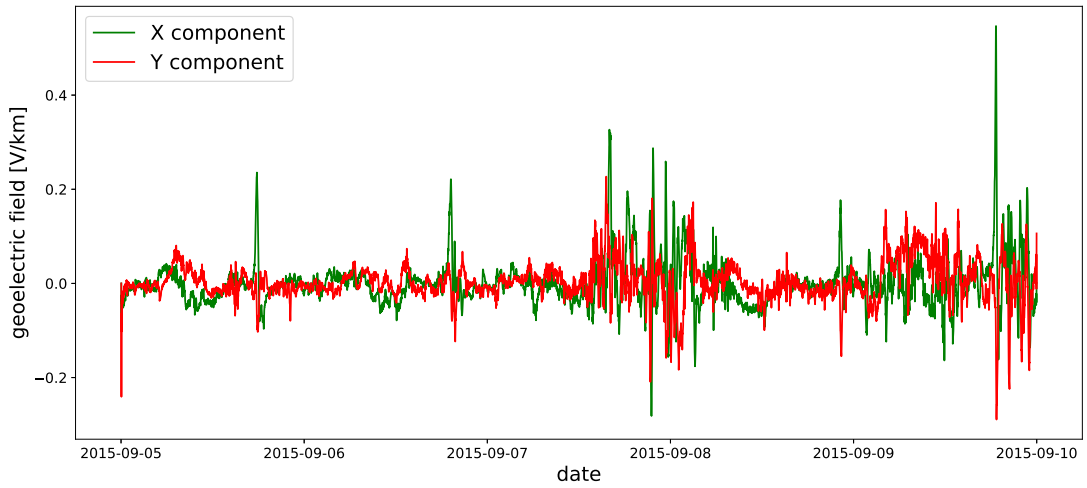

Figure A.13: North, X and East,Y components of the geoelectric field computed by the plane wave model using data from the Budkov Observatory from 5 to 10 September 2015.

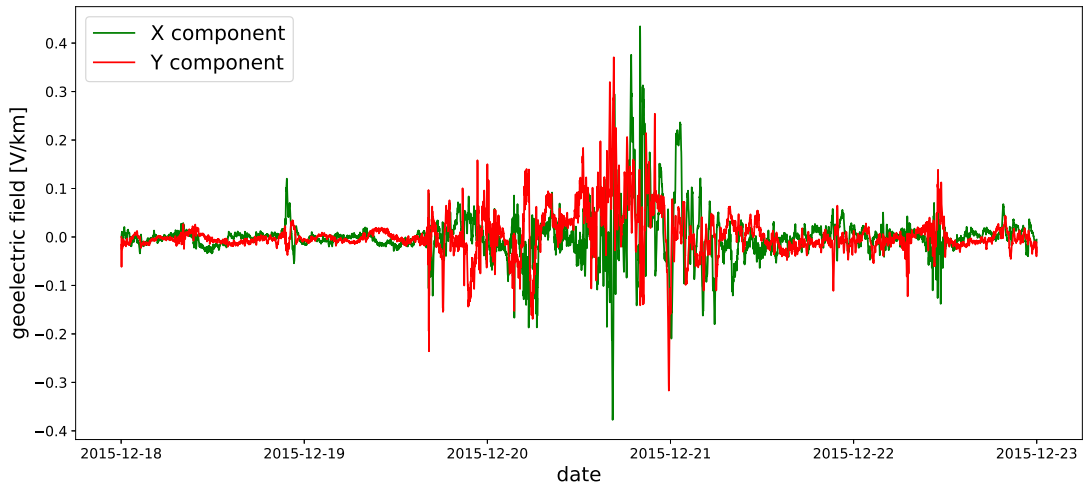

Figure A.14: North, X and East,Y components of the geoelectric field computed by the plane wave model using data from the Budkov Observatory from 18 to 23 December 2015.

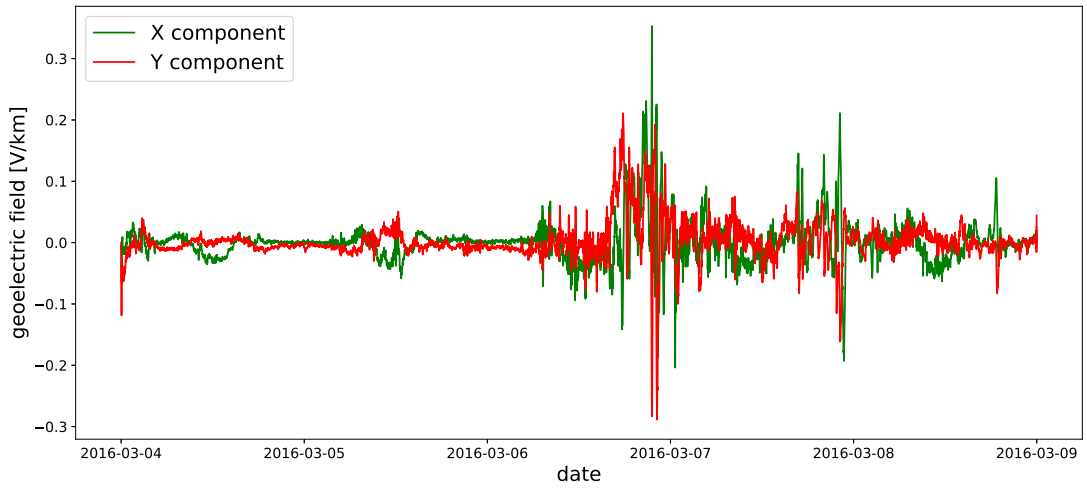

Figure A.15: North, X and East,Y components of the geoelectric field computed by the plane wave model using data from the Budkov Observatory from 4 to 9 March 2016.

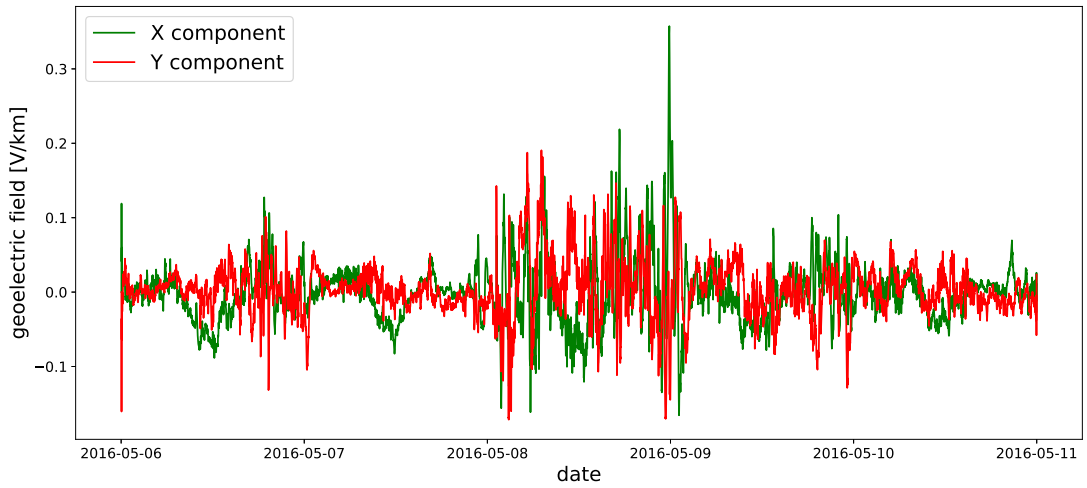

Figure A.16: North, X and East,Y components of the geoelectric field computed by the plane wave model using data from the Budkov Observatory from 6 to 11 May 2016.

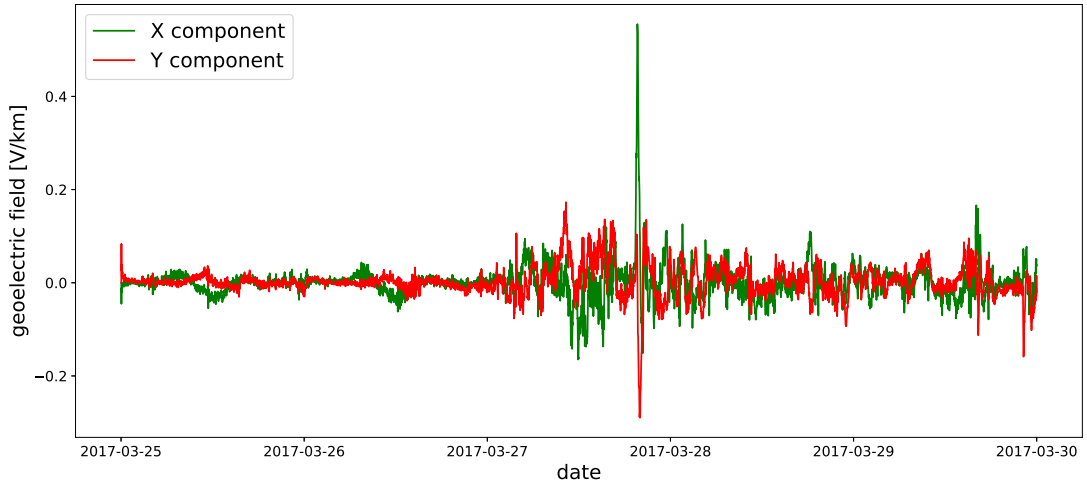

Figure A.17: North, X and East,Y components of the geoelectric field computed by the plane wave model using data from the Budkov Observatory from 25 to 30 March 2017.